Distinct neurogenic pathways shape the diversification and mosaic organization of cortical output channels

Shreyas M. Suryanarayana[1,5,*], Xu An[1,5], Yongjun Qian[1,2], Shengli Zhao[1], Hemanth Mohan[1,3], Z. Josh Huang[1,4,6,*]

[1] Department of Neurobiology, Duke University Medical Center, Durham, NC, USA

[2] Current affiliation: College of Future technology, Peking-Tsinghua Center for Life Sciences, IDG/McGovern Institute for Brain Research, Beijing Advanced Center of RNA Biology, Peking University, China

[3] Current affiliation:Department of Neurobiology and Anatomy, McGovern Medical School at UTHealth Houston, Texas, USA

[4] Department of Biomedical Engineering, Durham, NC, USA

[5] Co-first Authors

[6] Lead contact

*Correspondence: josh.huang@duke.edu;shreyas.suryanarayana@duke.edu

Summary

A hallmark of the mammalian cerebral cortex is its vast and diverse efferent projections across cortical areas mediated by extratelencephalic (ET) neurons that broadcast to myriad subcortical regions.
ET neurons are generated from two fundamentally distinct neurogenic pathways: direct neurogenesis (dNG-ET^d) from radial glia progenitors and indirect neurogenesis (iNG-ET^i) from intermediate progenitors, but the contribution of ET^d and ET^i to the organization of cortical output channels is unknown. Leveraging a novel lineage-based genetic strategy enabling differential viral access to ET^d and ET^i in the same mouse, we show that iNG-ET^i massively amplifies and diversifies dNG-ET^d across the cortex. While ET^d projections are largely restricted to the forebrain and midbrain structures, ET^i greatly amplifies and diversifies these projections and overwhelmingly dominates the innervation of hindbrain and spinal cord. This is exemplified in an area-specific pattern by ET^i dominance to brainstem and spinal action diversification and execution centers from motor areas, to major sensory processing stations along lemniscal pathways from sensory areas, and to pallial, hypothalamic and neuromodulatory structures from high order areas. Corticofugal subpopulations in multiple areas are derived from only ET^i, indicating the generation of novel projection types by iNG over dNG. Furthermore, area-specific ET^i, but not ET^d, spinal projection pattern is sculpted from the massive pruning of an early cortex-wide population during postnatal development. Together, these results uncover that two foundational neurogenic pathways with distinct evolutionary history differentially shape the area-specific diversification and mosaic organization of cortical output channels.

Introduction

The cerebral cortex is the crowning achievement of vertebrate evolution and contains a vast network of nerve cells underlying high-level brain functions from sensory processing to cognition and motor control [1–4]. Glutamatergic projection neurons (PNs) constitute up to 80% of cortical neurons and comprise several major classes characterized by their laminar location, projection patterns, and gene expression profiles [5–7]. Whereas the intratelencephalic (IT) neurons project within the cerebral hemisphere and mediate cortical processing streams, the extratelencephalic (ET) neurons constitute a massive and area specific efferent system that project to myriad subcortical targets throughout the central nervous system [6,8–10]. Decades of studies have uncovered daunting diversity in ET neuron projection patterns within and across cortical areas and across mammalian species [10–15]. Nevertheless, the same set of ET neurons are reliably generated in each animal to carry out species-typic behavioral functions, suggesting a stringent developmental genetic program. However, the development origin and process that shape ET projection diversity and their area specific profiles remain poorly understood.

All PNs, including ETs, are generated from radial glia progenitors (RGs) lining the embryonic cerebral ventricle through two fundamental forms of neurogenesis. In direct neurogenesis (dNG), a RG undergoes asymmetric division to self-renew and generate one neuronal progeny[4,16,17]; in indirect neurogenesis (iNG), RG first produces an intermediate progenitor (IP), which then undergoes symmetric division to generate two neurons[18–24]. Across the developing mammalian neural tube, dNG is ubiquitous from the spinal segments to the forebrain that generate the entire central nervous system, while iNG is largely restricted to the telencephalon that gives rise to the cerebral hemisphere[18,25]. Across vertebrate evolution, while dNG originated before the dawn of vertebrates and has been conserved ever since, iNG emerged largely since amniotes (but see [26]) and has expanded tremendously in mammals, and is thought to drive the evolutionary innovation of a 6-layered neocortex[20,23,25,27,28]. While the amplification of neuronal production through IPs is inherent to iNG, whether and how dNG and iNG differentially contribute to the diversification and organization of ET-mediated output channels is largely unclear.

Using a genetic strategy to distinguish and fate map dNG and iNG, we previously found that whereas dNG generates all major PN classes, iNG differentially amplifies and diversifies PNs within each class [17]. In particular, dNG and iNG generate ET^d and ET^i, respectively, which are completely intermixed in layers 5 and 6 and appear indistinguishable in gross dendrite morphology[17,29]. However, whether ET^d and ET^i differ in axon projection pattern – a crucial determinant of their connectivity and circuit function, remains unknown.

Here, we first establish a novel lineage-based genetic method that enables differential viral targeting of ET^d and ET^i in the same individual mice. Through systematic antero- and retrograde tracing of ET^d and ET^i across cortical areas, we show that iNG-ET^i massively amplifies and diversifies the dNG-ET^d projections across the cortex. While ET^d projections are largely restricted to forebrain and midbrain (MB) structures, ET^i greatly amplifies and diversifies these projections and overwhelmingly dominates the innervation of hindbrain and spinal cord (SpC) in an area-specific pattern. In particular, ET^i in motor areas dominate projections to brainstem (BS) and spinal action diversification and execution centers; ET^i but not ET^d in sensory areas expand projections to sensory processing centers along lemniscal pathways; and ET^i but not ET^d in higher order areas extend projections to other pallial structures and to hypothalamic and neuromodulatory centers. Corticofugal subpopulations in multiple areas are derived from only ET^i but not ET^d, indicating the generation of novel projection types by iNG over dNG. Furthermore, area-specific ET^i, but not ET^d, spinal projection pattern in mature cortex is sculpted from the massive pruning of an initial cortex-wide population during early postnatal period. Together, these results demonstrate

that two foundational neurogenic pathways with distinct evolutionary history seed the area-specific diversification and mosaic organization of cortical output channels that shape the central nervous system architecture.

Results

A genetic strategy enabling differential viral access to ET^d and ET^i in the same animal

To fully uncover the anatomical distinctions between ET^d and ET^i, we designed a novel genetic strategy that allows for differential viral targeting of these two subpopulations (**Figure 1A**). As currently there are no known gene expression differences between ET^d and ET^i, this strategy is based on their lineage distinction that resolves a common molecular marker. The zinc finger transcription factor *Fezf2* is broadly expressed in the majority of ETs including both ET^d and ET^i (Arlotta 2005, Matho 2021, Huilgol 2023), yet the T-box transcription factor *Tbr2* is selectively expressed in IPs that generate all PN^i, including ET^i but not ET^d [17]. Thus, we built a *FezF2-tTA-CreER (FezF2-TC)* knockin allele driving the conditional expression of two tandemly arranged cassettes: a tTA cassette flanked by Frt sequences followed by a CreER cassette (**Figure 1A**). We confirmed that *FezF2-TC* reliably captures endogenous *FezF2* expression pattern by *in situ* detection of *FezF2* mRNA in labelled ET neurons (**Figure S1A-C**). When combined with a *Tbr2-Flp* knockin allele [17], dNG-derived ET^d, which do not express *Tbr2-Flp* during development, will constitutively express tTA but not CreER; on the other hand, iNG and IP-derived ET^i, in which developmental expression of *Tbr2-Flp* removes the tTA cassette, will constitutively express CreER (**Figure 1A**). Thus, this genetic strategy converts developmentally transient lineage signals in neurogenesis to permanent "genetic handles" that allow differential viral targeting of postmitotic ET^d and ET^i in the same individual mice.

Indeed, retro-orbital co-injection of tTA-driven *AAV-TRE-GFP* and Cre-driven *AAV-FLEX-RFP* in *FezF2-TC;Tbr2-Flp* double transgenic mice resulted in reliable differential labeling of ET^d and ET^i respectively, across the cortex (**Figure 1B**). As negative controls, we verified that *AAV-FLEX-RFP* showed no leaky expression in the cortex (**Figure S1H-I**), and *AAV-TRE-GFP* showed minimal leaky expression that was restricted to somatic but not axonal labelling, even after immunofluorescence amplification (**Figure S1H-I**).

To further validate our strategy, we compared the numbers and relative ratios of AAV-based ET^d and ET^i labeling with those of a previously validated intersection-subtraction reporter allele (IS)-based labeling [17]. *AAV-TRE-GFP* and *AAV-FLEX-RFP* co-injection in motor, barrel, and visual cortex in *FezF2-TC;Tbr2Flp* mice yielded very similar labeling of ET^d and ET^i (**Figure 1D-F**) in equivalent areas in *FezF2-CreER;Tbr2-Flp;IS2* mice (**Figure 1G-I**). In both approaches, the number of ET^i neurons was significantly more than ET^d for motor and barrel cortices (**Figure 1D-F**), and there was no significant difference for the visual cortex although there were more ET^i neurons (**Figure 1F**). Although viral labeling captured greater number of ET^d and ET^i neurons in *FezF2-TC;Tbr2Flp* as compared to the IS2 reporter strategy, likely due to higher sensitivity of AAV labelling, there were no significant differences in their proportion, which ranged from 20-30% for ET^d (mean: 24.5%) and 70-80%for ET^i (mean:75.5%) for all three areas from either approach (**Figure 1G-I**). Thus, ET^d and ET^i are generated across different cortical areas with an overall ratio of approximately 1:3, indicating differential amplification by iNG. Together, these results validate our novel strategy for differential AAV targeting of ET^d and ET^i in the same animal.

Amplification, diversification and innovation of ET projection types by iNG

ET neurons are highly heterogenous, with diverse subcortical projection patterns that vary across isocortical areas. While ET^d and ET^i are distributed across different regions of the isocortex [17], whether and how they differ in their projection targets is unknown. We first addressed this question by retrograde labelling from four subcortical targets – the superior colliculus (SC), pontine nuclei (PONS), medulla (Med) and the SpC (**Figure 1A-D**). Given that the two retro-AAVs (*AAV-TRE-RFP* and *AAV-FLEX-GFP* that label ET^d and ET^i respectively) are co-injected in the same location in the same animal, this method allows us to compare the distribution and relative proportion of ET^d and ET^i across the isocortex. Brains were analyzed by both Confocal (n = 2, each target area, **Figure 2E-H**) and Lightsheet microscopy (n = 2-3 each target area, **Figure 2A-D** *bottom,* **S2E**, **Video S1-S4**). Indeed, retroAAV injection from the 4 target sites labeled intermixed layer 5 ET^d and ET^i that were distributed across the isocortex (**Figure 2A-D**, *bottom,* **S2A-D**).

Considering the overall proportions of ET^i and ET^d neurons across isocortex, the amplification of ET^i cell number over ET^d is approximately 3:1 (**Figure 1G-I *right***). If ET^i and ET^d neurons broadly project to the same sets of subcortical targets, we would broadly expect a similar degree of 3:1 *amplification* of ET^i over ET^d projection at these targets. However, retrograde labeling revealed a substantially disproportionate increase in L5 ET^i over ET^d proportion from all four injection sites (**Figure 2I-L *right***): the ET^i/ ET^d ratio ranged from 12.5:1 for collicular-projecting, 25:1 for pontine-projecting, 33:1 for medullary-projecting, to 40:1 for spinal-projecting neurons. As each ET neuron often projects to different combinations of these targets, this result indicates a substantial *diversification* of projection patterns for ET^i over $ET^{d,}$, especially those to the more distal targets assessed. Moreover, while both ET^i and ET^d neurons were always co-labeled and intermixed across areas, though at different ratios, by colliculus injection, there were multiple areas (e.g., SSp-n, AUDpo, ORBv, ILA) where only ET^i but not ET^d neurons were labeled by injection to the PONS, Med, and SpC (**Figure 2M-O**). This result indicates the presence of novel distally-projecting ET types in these areas generated only through iNG, which we consider as *innovation* by iNG (**Figure 2P**). Notably, these novel area-specific ET^i projection types were largely found in sensory and higher order areas rather than motor areas (**Figure 2M-O**). This result suggests that in addition to the diversification of ET projection types from the frontal and motor areas, iNG generates novel projection types in some non-motor areas that give them direct access to the motor centers and other areas in the PONS, Med and SpC.

Although the 4 injection sites represent only a small subset of ET targets, the results together demonstrate that, compared with dNG, iNG not only amplifies but also diversifies projection classes, and additionally generates novel projection types. To reveal the precise and comprehensive projection patterns of ET^d and ET^i in specific areas, we then carried out a set of anterograde labeling across eight isocortical areas encompassing motor, sensory, and higher order areas.

ET^i in motor areas expands projections to action diversification and execution circuits

For the motor areas, we chose the rostral forelimb orofacial area (RFO [30]) and the caudal forelimb area (CFA [11,31–33]) in the primary motor cortex (MOp) and an area in the secondary motor cortex (MOs) recently implicated in a forelimb-reach-to-grasp behaviour [34](**Figure 3A-C *top***, **S3A, S4A, S5A**). In all three areas, *AAV-TRE-GFP* and *AAV-FLEX-RFP* labelled ET^d and ET^i in deep layers, with approximately 1:3 ratio (**Figure S3A1-A2, S4A1-A2, S5A1-A2**). Our goal here is to quantitatively compare the relative strength of ET^i and ET^d projections across major subcortical targets. While confocal microscopy gave high resolution view of subsets of targets (n = 2 for each area, **Figures S3A-G, S4A-G, S5A-G**), light-sheet microscopy enabled us to capture the entire projections to all targets in the whole brain (n = 2 for each area, **Figure 2A-C, S3H, S4H, S5H, Video S5-S7**). We generated 3D renderings of projections and

fraction occupation heatmaps for all downstream targets (listed in **Table S1**) for the 3 injection areas (**Figure 3A-C, 3D-F**).

To quantify the relative projection strength of ET^i and ET^d using light-sheet microscopy datasets, we measured the percent occupancy in selected target structures using ET^d or ET^i axon fluorescence signals. This measurement is not in terms of fluorescence intensity, which is not directly comparable between tdTomato (ET^i) and GFP (ET^d), and could be an underestimate of ET^i projection strength. An equivalent ratio of ET^i over ET^d projection strength to that of their cell body ratio at injection site (e.g. 3:1) would suggest a simple amplification by ET^i. On the other hand, a disproportional increase of ET^i proportions at different target regions would suggest a diversification or innovation of ET^i projections. Thus, in addition to assessing the relative increase of ET^i over ET^d projections at each target, we compared them across different target regions of interest and ran post-hoc comparisons between these regions with the thalamus to reveal specific target regions with a disproportional increase of ET^i projections. The thalamus was chosen for comparison as a forebrain region which receives substantial ET^d as well as ET^i projections.

While both ET^d and ET^i targeted the thalamus (**Figure S3B, S4B, S5B**), ET^i had significantly more projections from all three areas (**Figure S3B1-B3, S4B1-B3, S5B1-B3**). Notably, *FezF2* expressing ET neurons include both PT (pyramidal-tract like, mostly in L5b but also L6) and some CT (cortico-thalamic in L6) populations; thus, labeled thalamic projections derive from both populations (See Discussion, **Figure S3B, S4B, S5B**).

As a broad category, projections to the brainstem areas (i.e. PT type projections that include MB, PONS, Med, SpC) from all three motor areas were significantly amplified in ET^i over ET^d (**Figure S3B1-B3, S4B1-B3, S5B1-B3**). Within the thalamus, the three motor areas showed differences in ET^d vs ET^i projection to first order (FO) and higher order (HO) nuclei. RFO and MOs had similar ET^d and ET^i projections to FO but more ET^i projections to HO (**Figure S3C1-C3, S5C1-C3**). CFA had stronger ET^i projections to both FO and HO (**Figure S4C1-C3**).

At the level of basal ganglia (BG), ET^i had a major enhancement of projections over ET^d to all BG nuclei from all three areas (**Figure S3D1-D3, S4D1-D3, S5D1-D3,Figure 3G-I**) indicating vastly expanded control by ET^i over action selection circuits [35,36].

In the MB, ET^i had significantly more projections than ET^d from all three areas (**Figure S3E1-E3, S4E1-E3, S5E1-E3**); this was also true for projections to the PONS and Med (**Figure S3F1-F3, S3G1-G3, S4F1-F3, S4G1-G3, S5F1-F3, S5G1-G3)**. When the relative increase of ET^i over ET^d was compared across target regions, there were significant differences (p value for RFO:$p < 0.05$; CFA:$p < 0.0001$; MOs:$p < 0.01$, Kruskal–Wallis test). Post-hoc comparisons revealed that for all three areas, increase of ET^i over ET^d to the Med and BG and additionally to PONS were more pronounced, compared to that in thalamus (**Figure S3H, S4H, S5H**). This result suggests that Med-projecting ET from RFO and PONS- and Med- projecting ET from the CFA and MOs are largely generated by iNG.

Thus, across motor areas, while both ET^d and ET^i target forebrain and midbrain areas, the bulk of corticofugal projections to more distal targets are predominantly generated by iNG-ET^i to innervate action selection, diversification and execution centers in the BG, hindbrain and SpC, (**Figure 3G-I**). This expansion by iNG-ET^i thus creates the anatomical substrate for monosynaptic control of motor centers in the BS and SpC by motor areas of the isocortex.

ET^i in sensory areas expands subcortical projections to ascending sensory pathways

We targeted three sensory areas for anterograde tracing – the visual cortex (VIS), auditory cortex (AUD) and barrel cortex (BAR) (n=2 [confocal, **Figure S6A-E, S7A-G, S8A-G**], n = 2 [Lightsheet, **Figure S6F, S7H, S8H, Video S8-S10**] for each area, **Figure 4A-C *top*, S6A, S7A, S8A**). The VIS injection labelled neurons in layers 5 and 6 with more ET^i (**Figure S6A1-A2, S7A1-A2, S8A1-A2**). In AUD and BAR areas, there were more ET^i labelled in layer 5; while in layer 6a/6b, more ET^d or near equal numbers of ET^d and ET^i were labelled (**Figure S7A1-A2, S8A1-A2**). The larger number of ET^d in layer 6a/6b are likely CT neurons, which are mostly derived from dNG [17]. We generated 3D renderings of projections and heatmaps for all three injection areas (**Figure 4A-C, 4D-F**).

From VIS and AUD, there was significantly more ET^i than ET^d projections to both the thalamus and brainstem areas (**Figure S6B1-B3, S7B1-B3, S8B1-B3**). Within the thalamus, there was no significant difference between ET^d and ET^i projections to FO while ET^i had significantly more projections to HO (**Figure S6C1-C3, S7C1-C3, S8C1-C3**). The dense projections of ET^d to FO may include a significant CT component while those of ET^i to both FO and HO could largely derive from PT.

For AUD and BAR areas, we compared ET projections to major sensory processing stations along their respective ascending lemniscal pathways. ET^i but not ET^d heavily targeted lemniscal centers, suggesting that iNG confers sensory cortical access to lemniscal sensory processing centers (**Figure S7D1-D3, S8D1-D3**).

When examining VIS corticofugal projections, we noticed that in some prethalamic nuclei such as the ventral lateral geniculate (LGv), the ET projections were almost entirely ET^i (**Figure S6C**). Notably, LGv is expanded in nocturnal mammals such as rodents and is similar in size to the LGd [37].

Regarding ET projections to the MB, projections from all three areas were dominated by ET^i (**Figure S6D1-D3, S7E1-E3, S8E1-E3**). There were generally more ET^i than ET^d projections to PONS and Med (**Figure S6E1-E3, S7F1-F3, S7G1-G3, S8F1-F3, S8G1-G3**). Notably, the relative increase of ET^i over ET^d for VIS was not different between target regions indicating a similar increase of ET^i projections across subcortical structures (**Figure S6F**). In contrast, the increase of ET^i over ET^d from AUD for the lemniscal centers and PONS was larger than that in the thalamus (**Figure S7H**); this was true across the BS for BAR (**Figure S8H**).

Thus, in sensory areas, iNG-ET^i elaborates projections to HO, prethalamus and sensory lemniscal centers, while also incorporating motor like features to BAR with elaborated projections to hindbrain. In contrast, ET^d heavily targets FO, with projections also to the midbrain and weak projections to lemniscal centers, PONS and Med (**Figure 4G-I**).

ET^i in higher order areas diversifies projections to pallial, hypothalamic and neuromodulatory structures

We further compared ET^i and ET^d projections in two higher order areas of the isocortex, the prefrontal (PFC) and posterior parietal areas (PAR) (n=2 for confocal, [**Figure S9A-J, S10A-G**], n = 2 for Lightsheet, **Figure 5A-B, S9K,S10H,Video S11-S12**] for each area**.** The injection at each area labelled neurons with more ET^i than ET^d (**Figure S9A-A2, S10A-A2**, **Figure 5A-B, 5C-D**).

From the PFC, both ET^i and ET^d targeted the thalamus heavily while there were stronger ET^i projections over ET^d to the brainstem regions (**Figure S9B1-B3**). In contrast, from PAR,there were more ET^i projections over ET^d to both thalamus and BS, similar to what was observed in motor areas (**Figure S10B1-B3**). This result suggests higher numbers of PT neurons in PAR sending collaterals to thalamus.

Comparing projections to FO and HO thalamus, from PFC ET^d had stronger projection to FO than ET^i, while ET^i had stronger projection to HO. From PAR, there were stronger ET^i projections to both FO and HO (**Figure S9C1-C3, S10C1-C3**). The PAR projections to FO and HO were similar to proportions of ET^i and ET^d projections from motor areas (**Figure S10C1-C3**). Given this similarity and since the PAR is known to have roles in motor behavior [38,39], we further examined BG and found that again that the projections were predominantly ET^i **(Figure S10D-D3)**.

The PFC is known to target multiple non-isocortical pallial areas [40]. We found that the majority of these projections were ET^i (**Figure S9D1-D3**), suggesting a massive elaboration of inter-pallial interaction by iNG- ET^i. Some other forebrain areas like the epithalamus received similar PFC ET^d and ET^i projections (**Figure S9E1-E3**). Notably, ET^i projections dominated the hypothalamus (**Figure S9F1-F3**). This highlights selective expansion of projections by distinct neurogenic mechanisms in anatomically/developmentally close and related structures.

Another important observation was the heavy ET^i over ET^d projections to different neuromodulatory centers across the brain from PFC (**Figure S9G1-G3**), indicating the expansion of higher order cortical control of neuromodulation. PFC and PAR projections to the MB and PONS were largely ET^i (**Figure S9H-H3, S9I-I3, S9J-J3, S10E-E3, S10F-F3, S10G-G3**).

Taken together and considering the relative increase of ET^i over ET^d among different target regions and the thalamus, ET^i in higher order areas selectively expands projections to neuromodulatory centers, hypothalamus and also dominates interactions with other pallial areas while incorporating motor area like features with significant expansions to hindbrain and SpC (**Figure S9K, S10H, Figure 5E-F**).

Selective axon pruning in ET^i but not ET^d during early postnatal development shapes the areal distribution of ET^i

The area specific ET projection patterns to multiple subcortical regions are established by a multi-step developmental process that involves progressive (axon guidance, synapse formation) as well as regressive (axon pruning, synapse elimination) events [41,42]. In particular, axon pruning has been demonstrated for corticofugal neurons from multiple cortical areas during early postnatal period [43], with a prominent role in shaping the arealization of descending pathways [44]. We therefore examined whether axon pruning may differentially sculpt the projection patterns and arealization of ET^d and ET^i. As substantial pruning of mouse corticospinal axons occurs during the first postnatal week, we injected retroAAVs in the cervical spinal cord (cSpC) of P4 mice and examined cortex-wide ET^d and ET^i labelling pattern at P40 (P4-P40), and compared it with those labeled from adult (P28) cSpC injection (P28-P40) (n = 2 [confocal, **Figure 6C-D**], n = 2 [Lightsheet, **Figure 6A-B, S11D, Video S13**]).

In contrast to the P28-P40 ET labeling pattern that is highly restricted to a few areas (MOp, MOs, SSp, **Figure 6E**), P4 cSpC injection labeled a significantly larger number of ET neurons across the anterior-posterior extent of cortex (**Figure 6F-G**), consistent with previous findings(Abe et al., 2024; Stanfield et al., 1982). Strikingly, this vast expansion of P4-P40 ET labeling consists of almost exclusively ET^i (**Figure 6H-I**). In contrast, P4-P40 labeled a small number of ET^d neurons that remained restricted to the same few areas as those in P28-P40 labeling (**Figure 6F-I**). This result suggests that across the early postnatal cortex, ET^i, but not ET^d, initially project to the spinal cord; and the massive cortex-wide pruning of ET neuron axons that sculpts their subsequent areal specific patterns is restricted to ET^i. In contrast, most ET^d neurons across the developing cortex do not project to the spinal cord, and the mature pattern of ET^d-spinal projection in specific areas (e.g. MOp, MOs and SSp) is likely achieved by area-specific properties of axon growth and guidance.

Notably, ET neurons reside in both L5 and L6, and many L6 ET neurons project to more proximal subcortical targets than the spinal cord. In this context, we found that P4 cSpC injection labeled many L6 ET^i but not ET^d in MOs and SSs (**Figure 6J-K**). This result suggests that the corticofugal projection pattern of L6 ET^i, but not ET^d, is shaped by the pruning of their axon arbors that initially reached the spinal cord.

Surprisingly, we found that P4 cSpC injection further labeled iNG- but not dNG-derived neurons in many pallial areas outside of the isocortex (**Figure S11A-C, S11E-G**). The largest number were found in the hippocampal formation (**Figure S11C, S11E**) but also in other regions including piriform cortex (**Figure S11A**) and amygdala (**Figure S11B**). As controls, cSpC injection at P1, when ET axons have not reached the spinal cord, resulted in very sparse labelling of ET^d and ET^i in cortical structures at P40 (n = 2, **Figure S11G**). Further, sSpC injection of a generic retro-AAV into wild type mice at P6 labeled neurons in both the neocortex and other pallial areas, confirming our results using *FezF2TCTbr2Flp* mice and Cre and tTA dependent retro-AAvs (n = 2, **Figure S11I**). All together, these results suggest that an initial exuberant axon growth, many reaching the SpC, followed by extensive pruning, is a general feature of ET^i but not ET^d across the pallial/cortical structures to establish their areal specific subcortical projection patterns.

Discussion

The mammalian cerebral cortex contains a vast neural network comprising dozens of functional areas, which together integrate sensory information with cognitive and internal state signals to guide behavior. The computational outcome of each cortical area is broadcast to multiple subcortical regions by diverse subpopulations of ET neurons. Decades of studies demonstrate that ET projection patterns vary substantially within as well as across cortical areas and across mammalian species [5,8–10,45,46]. It has remained an enigma whether this daunting and seemingly unresolvable heterogeneity is stochastic, reflects a continuum, or can be meaningfully classified into ground truth subpopulations relevant to systems level organization and function. Here we dissect the diversity and organization of ET neurons based on a fundamental distinction in their developmental origin – dNG and iNG, which differ not only in progenitor cell types (RG vs IP), cell division patterns (asymmetric vs symmetric), and distribution along the neural tube, but also in evolutionary history. A key experimental entry point is our design of a genetic strategy that converts developmentally transient lineage signals in neurogenesis to permanent “genetic handles” that allow differential viral targeting of postmitotic ET^d and ET^i in the same individual mice. We found that ET^d projections are largely restricted to forebrain and midbrain structures, while ET^i differentially amplifies and diversifies these projections in an area-specific way across brain systems, and overwhelmingly dominates the innervation of hindbrain and spinal cord. Importantly, corticofugal subpopulations in multiple areas are derived from only ET^i but not ET^d, indicating the generation of novel projection types by iNG over dNG. Furthermore, areal-specific ET^i, but not ET^d, spinal projection pattern is sculpted from the massive pruning of an initial cortex-wide population during early postnatal period, and spinal axon pruning is a common feature of ET^i over ET^d across broadly defined cortical structures. Together, these results uncover that two foundational neurogenic pathways with distinct evolutionary history differentially shape the area-specific diversification and mosaic organization of cortical output channels (**Figure 7**).

A developmental and evolutionary (i.e. evo-devo) perspective is uniquely informative in interpreting and understanding the major differences in ET^d and ET^i projection patterns and provides deep insights into the basic organization of the ET cortical output system. In early vertebrates, the ancient pallium already evolved a blueprint of projections to downstream motor centers [47], with several cardinal cell types [48] and

basic connectivity[49], but the overall behavioral repertoire was limited and the involvement of pallium in motor control was rudimentary [1,50]. The motor centers in the midbrain tectum (superior colliculus) [51], tegmentum and the well conserved BG in the forebrain [52], played key roles in motor control and behavior [53]. With the emergence of amniotes (reptiles and mammals), the "higher order" orchestration of motor control has gradually shifted from downstream motor centers to the cortical pallium [54,55], culminating in the mammalian isocortex. In parallel with the evolution of limbs, hands and digits, command centers for specialized movements expanded in the midbrain, BS, and SpC [56–58]. The mammalian isocortex in particular, has seen a massive elaboration of efferent projections, giving it increasing monosynaptic access and control of these downstream motor centers, culminating with monosynaptic projections to the SpC, which in primates targets spinal motor neurons [8,59]. Importantly, this momentous shift of high-level motor control from the tectum to the isocortex is mediated by the vastly expanded and diversified ET corticofugal projections and is correlated with the evolutionary expansion of iNG. While the amplification of neuronal production to expand cortical size is inherent to iNG, a major question is whether and how dNG and iNG differentially contribute to the diversification and organization of neuron types, in particular ET neurons that mediate cortical output channels that drive brain function and behavior. Our basic premise is that the mouse dNG-ET^d represents the mammalian instantiation of the evolutionarily more ancient system that has been conserved (albeit updated) across vertebrates, while iNG-ET^i represents the mammalian expansion and innovation. We posit that these two parallel systems form mosaic circuits with functional relevance, each reflecting its evolutionary history. This evo-devo framework allows us to infer how dNG-ET^d and iNG-ET^i shape the basic organization and function of the ET system by considering major species differences in body, brain, and behavior across vertebrates.

Across different cortical areas and functional systems, ET^d and ET^i projections from the motor areas present strong interpretations for their functional distinction in the context of the evolution of vertebrate motor control systems [1,60,61]. The RFO coordinates orofacial and forelimb actions in food manipulation, and CFA mediates forelimb movement —both via FezF2-expressing ET neurons (An et al., 2022;[33,38,62,63]. Thus, iNG-ET^i expansion may enable motor cortex control of complex oromanual and forelimb behaviors. MOs, a higher-order motor area involved in decision-making across sensory modalities ([64–66], also shows iNG- ET^i projections to BS and SpC. We further reveal strong iNG-ET^i input to all BG nuclei, including GPe [67] and output nuclei [68], which regulate action selection, instrumental behaviors, and habit formation [35,69,70]. This may support cortical modulation of BG circuits during motor learning [71] and habit formation [72] or allow cortical override of BG-driven action selection ([36,73]. ET^i /ET^d ratio increases along proximal to more distal targets —from collicular to spinal targets —suggesting iNG-ET^i diversification enhances direct cortical control of BS motor centers. Our findings suggest that dNG-ET^d mainly regulate movement via forebrain and midbrain innervation, while iNG-ET^i expands and diversifies outputs across BS and SpC. This iNG-ET^i cortical innovation enables skilled, flexible forelimb behaviors. In primates, further iNG-ET^i elaboration may underlie monosynaptic corticospinal-motor neuron connections for fine digit control [8,45].

Sensory areas also show expanded iNG-ET^i projections. ET^d neurons are equally or more abundant than ET^i in layer 6, likely reflecting that CT neurons expressing Tle4 [74] originate from dNG (Huilgol et al., 2023). FezF2 recruits Tle4 to repress PT genes, and their co-expression in layer 6 [75] likely explains their labeling. BAR areas exhibit both strong CT (ET^d) input to FO and extensive PT (ET^i) projections to HO, BS, and SpC. As a rodent-specific sensorimotor area [76], BAR may exemplify evolution of hybrid output pathways via distinct neurogenic programs, consistent with isocortical expansion of sensory, motor, and cognitive functions through arealization [3,77,78].VIS shows strong ET^i and minimal ET^d projections to GABAergic prethalamic nuclei like vLGN, expanded in nocturnal mammals [37] and mediating innate visual behaviors

such as fear [79,80]. VIS input to vLGN can suppress such responses [81], exemplifying iNG-ET^i diversification enabling the sensory cortex to modulate instinctive behaviors through learning. iNG-ET^i expansion in sensory areas also targets lemniscal pathway centers. In BAR, PT (ET^i) neurons project to structures such as principal trigeminal nucleus (barrelettes, [82] and VPM (barreloids, [83]); in AUD, to the superior olive (sound localization, [84]) and inferior colliculus (acoustic-motor functions, [85]). These projections allow cortical modulation of sensory processing at multiple levels, unlike dNG-ET^d.

In higher-order areas, PAR—located between somatosensory and visual cortices—supports decision-making and movement planning [38,86,87], and shows expanded ET^i output to BG, BS, and SpC. PFC, the most recently evolved isocortical area, supports cognitive control [88]. It shows ET^i projections to pallial targets like BLA and hippocampus, critical for social behavior and memory [89–92], and to neuromodulatory centers like the VTA and dorsal raphe, influencing reward and behavioral states [93]. ET^i projections to the hypothalamus also support sleep [94], aggression, and stress responses [95]. Altogether, the results reveal the mosaic organization of dNG-ET^d and iNG-ET^i projection streams across motor, sensory and higher order areas. They indicate that iNG-ET^i is key to form area-specific projections from different isocortical areas, establishing their identity and function. They further suggest how the rise and arealization of iNG-ET^i across the isocortex have re-shaped the rest of the central nervous system architecture through their massive and areal-differentiated corticofugal projections (**Figure 7**).

The area-specific corticofugal projection patterns of ET neurons are likely achieved by the interplay of two broad classes of developmental mechanisms involving progressive as well as regressive processes. While genetic programs for targeted axon growth and guidance are well-suited to specify a species-invariant projection scaffold, regressive axon pruning allows for refinement of initially more exuberant branches, possibly in an activity- and utility-dependent manner to sculpt functional connections ([41]). In particular, axon pruning has been implicated in the establishment of ET projection patterns [43]. ET neurons across broad cortical areas initially all extend their axons distally to the spinal cord, then undergo massive axon pruning to sculpt their subcortical projection patterns and area specific distribution [4443], [44]. A recent study examined axonal pruning on two broad subpopulation of ET neurons: ET$_{dist}$ that predominate in the motor cortex and project distally to the pons, medulla and SpC, and ET$_{prox}$ that predominate in visual cortex and project more proximally to pons and thalamus [12,44]. Whereas subsets of ET$_{prox}$ emerge from pruning of their initially distal-projection axons, others emerge through target growth. Here, we found that, across the developing early postnatal cortex, it is largely the ET^i neurons that extend their axons the spinal cord, which then undergo massive pruning to achieve areal specific patterns. In sharp contrast, most developing ET^d across the cortex do not extend axons to the spinal cord, with the exception of a small subset largely restricted to motor areas. Notably, within the developing secondary motor and somatosensory areas, L6 in addition to L5 ET^i axons also project to the SpC, which are subsequently pruned. Furthermore, beyond the isocortex, broadly defined Fezf2-expressing ET^i but not ET^d neurons in other cortical structures (e.g. hippocampus, BLA, entorhinal cortex, etc) also initially project to SpC and then undergo pruning. Although we cannot rule out the possibility that a subset of ET^d neurons that project to more proximal targets also undergo pruning, our results indicate that exuberant axon growth followed by extensive pruning is a general and key feature that distinguish ET^i from ET^d. It is plausible that regressive axon pruning is an effective mechanism to sculpt projection patterns customized to individual animals in part through use- and activity-dependent mechanisms.

Beyond axon projection patterns, our reliable experimental access to dNG-ET^d and iNG-ET^i will enable multi-faceted analysis of these developmental genetic-defined subpopulations. Future studies will trace their synaptic input patterns, record and manipulate their activity during behavior, and reveal their gene

expression profiles and regulatory programs. These studies will integrate the developmental genetic and systems neuroscience approaches toward understanding the diversity and organization of cortical neuron types in the context of vertebrate evolution.

Acknowledgements

We thank Dr. Dhananjay Huilgol and Dr. Yi Li for helpful discussions. We are indebted to Leah Chestnut and Aditi Patel (LifeCanvas Technologies) for their excellent work on Lightsheet Microscopy Imaging. Funding: NIH grant U19MH114823-01 (ZJH). NIH Director's Pioneer Award 1DP1MH129954-01 (ZJH). International Postdoc Grant, Swedish Research Council grant no: 2021-00238 (SMS).

Author Contributions

ZJH and SMS conceived of the study. SMS, ZJH, XA designed experiments. SMS and XA performed the experiments. YQ designed the *FezF2-TC* mouse line. SZ made the AAV viruses. SMS analyzed the data with inputs from XA and HM. SMS and ZJH wrote the manuscript. ZJH supervised all aspects of the study and provided the funding.

Declaration of interests

The authors declare no competing interests.

Inclusion and diversity

We support inclusive, diverse, and equitable conduct of research.

Methods

Resource availability

Lead contact

Further information and requests for resources and reagents should be directed to and will be fulfilled by the lead contact, Z. Josh Huang (josh.huang@duke.edu).

Materials availability

Materials generated in this study are available on request to the lead contact. *FezF2-TC* mice generated in this study will be deposited to Jackson Laboratory.

Experimental model and study participant details

We have used adult mice (*Mus musculus*) in this study. Adult male and female mice bred onto a C57BL/6J background were used in the experiments. All mouse colonies were maintained in accordance with husbandry protocols approved by the IACUC and housed by gender in groups of 2–5 with access to food and water ad libitum and on a 12-hour light/dark cycle. The experimental procedures were approved by the Institutional Animal Care and Use Committee of Duke University and performed in accordance with the US National Institutes of Health (NIH) guidelines. All adult mouse histology experiments were performed on or after postnatal day P28-P40 animals. Postnatal experiments were performed on P1-P6 mice. We have used the following knock-in mice in this study: Driver lines include *FezF2-tTA-CreER* (this

study);*Tbr2-2A-FlpO* (MGI:752305); *Fezf2-2A-CreER* (RRID:IMSR_JAX:036296). Reporter lines include *Intersection-Subtraction (IS2)* (RRID: IMSR_JAX:036760) and *LSL-Flpo* (IMSR_JAX:028584). Mouse related experimental procedures were approved by the Institutional Animal Care and Use Committee (IACUC) of Duke University in accordance with NIH guidelines.

Method details

Generation of *FezF2-tTA-CreER* knock-in mouse line

FezF2-tTA-CreER was generated by inserting a *frt-tTA-frt-CreER* cassette in frame before the STOP codon of *FezF2*. In *FezFTC;Tbr2-Flp* double-allele mice, dNG-derived ET^d express *tTA* while iNG-derived ET^i express *CreER*, as *tTA* is removed by *Tbr2-Flp* in IPs. Postnatal injection of *AAV-TRE-GFP* and *AAV-FLEX-RFP* in cortex differentially label ET^d and ET^i respectively. Targeting vectors were generated using a PCR-based cloning approach as described before [17,96,97].

Tamoxifen induction

Tamoxifen (T5648, Sigma) was prepared by dissolving the powder in corn oil (20 mg/ml) and constant magnetic stirring overnight at 37°C. A 100–200 mg/kg dose was administered by intraperitoneal injection at the appropriate age; If two doses, 100mg/kg doses were administered at P21 and P28. For experiments with early postnatal mice, it was administered intraperitoneally at P5-P14 from a diluted stock of 5mg/ml. For *FezF2TC;Tbr2Flp* mice with viral infections, tamoxifen induction was performed via intraperitoneal injections at a dose of 100 mg/kg with the first induction after one day following the viral infection and subsequently every 2-3 days, 2-3 times.

Immunohistochemistry

Adult mice were anaesthetized (using Isoflurane) and transcardially perfused with phosphate buffered saline (PBS) followed by 4% paraformaldehyde (PFA) in 0.1 M PBS. Post-fixation, brains were rinsed three times in PBS and sectioned at a 65-70μm thickness with a Leica VT1000S vibratome. Sections were treated with a blocking solution (10% normal goat serum and 0.2% Triton-X100 in 1X PBS) for 1h, then incubated overnight at 4°C with primary antibodies diluted in the blocking solution. Sections were washed three times in PBS and incubated for 2h at room temperature with corresponding secondary antibodies, Goat or Donkey Alexa Fluor 488, 594 or 647 (1:500, Life Technologies) and DAPI or Blue/Far-Red Neurotrace fluorescent Nissl stain to label nuclei (1:1000 in PBS, Life Technologies, 33342, Molecular Probes N21479). Sections were washed three times with PBS and dry-mounted on slides using Fluoromount-G (SouthernBiotech, 0100-01) mounting medium.

In situ hybridization

Hybridization chain reaction (HCR) in situ was performed as previously described(Choi et al., 2018). *FezF2* probes were ordered from Molecular Instruments. Mouse brains were sliced into 50-μm-thick slices after paraformaldehyde (PFA) perfusion fixation and sucrose protection. HCR in situ was performed via the free-floating method in a 24-well plate. First, brain slices were exposed to a probe hybridization buffer with HCR Probe Set at 37 °C for 24 hours. Brain slices were washed with a probe wash buffer, incubated with amplification buffer and amplified at 25 °C for 24 hours. On day 3, brain slices were washed, counter-stained with DAPI/Nissl and mounted. *FezF2* (546 nm) probes were used to label *FezF2*+ neurons.

Viral vectors

All viral vectors were produced in house. Viral Vectors used: *AAV9-CAG-FLEX-tdTomato*, *AAV9-TRE3G-EGFP, AAVPHP.eB-TRE3G-EGFP, AAVPHP.eB-CAG-FLEX-tdTomato, AAVretro-TRE3G-mScarlet, AAVretro-CAG-DIO-EGFP, AAVretro-TRE3G-H2B-mScarlet, AAVretro-CAG-DIO-H2B-EGFP, AAVretro-CAG-EGFP*. All viral vectors were aliquoted and stored at -80 °C until use.

Stereotaxic surgery

Mice, anesthetized with isoflurane (2-5 % at the beginning and 0.8-1.2 % for the rest of the surgical procedure), were positioned in a stereotaxic frame and their body temperature was maintained at 34-37 °C with a heating pad. Lidocaine (2%) was applied subcutaneously to the scalp prior to surgery. Ketoprofen (5 mg/kg) was administered intraperitonially (IP) as an analgesic before and after surgery. A vertical incision was made through the scalp and connective tissue to expose the dorsal surface of the skull. The skin was pushed aside, and the skull surface was cleared using saline. A digital mouse brain atlas, linked to the stereotaxic frame, guided the identification and targeting of different brain areas (Angle Two Stereotaxic System, Leica Biosystems). A small burr hole was drilled in the skull and brain surface was exposed. A pulled glass pipette, with a tip of 20-30 µm, containing the viral suspension was lowered into the brain. A 500-700 nl volume was delivered at a rate of 10-30 nl/min using a Picospritzer (General Valve Corp). The pipette remained in place for 5 min, to prevent backflow, prior to retraction. The incision was closed with Tissueglue (3M Vetbond) and 5/0 nylon suture thread (Ethilon Nylon Suture, Ethicon). The mice were kept warm on a heating pad during recovery. Coordinates used are as follows (all measured in mm from bregma except for medulla):

Area	Anterior/Posterior (+/-,mm)	Lateral/Medial (+/-,mm)	Dorsal/Ventral (+/-,mm)
Rostral forelimb orofacial area (RFO)	1.71	2.25	-0.65
Caudal forelimb area (CFA)	0.5	1.5	0.6
Secondary motor cortex (MOS)	1.6	1.37	-0.7
Visual Cortex (VIS)	-3.4	2.6	0.55
Auditory Cortex (AUD)	-2.6	4	-0.95
Barrel Cortex (BAR)	-1.1	3.1	-0.6
Prefrontal Cortex (PFC)	1.7	0.4	-1.5
Parietal Cortex (PAR)	-1.85	1.3	-0.6
Superior Colliculus	-3.68	0.5	-1.6
PONS	-4	0.5	-5.5

Medulla [measured from Lambda]	-1.4	1.55	-4.3

Injections into the spinal cord of adult mice were performed as described [98]. Specifically, a dorsal incision was made along the vertebral column at the cervical level. The overlying muscle was dissected to expose the cervical vertebral column, and a laminectomy was performed at C5-7 to expose the spinal cord. 0.5 µl of viral solution was injected at 0.4 mm lateral to midline and 0.5 mm and 1 mm depth using a glass micropipette. The dorsal muscle layers were sutured, and the skin was closed with sterile wound clips. For all anterograde and retrograde injections, a viral suspension containing a mixture of *AAV9-CAG-FLEX-tdTomato* and *AAV9-TRE3G-EGFP* or *AAVretro-CAG-DIO-EGFP* and *AAVretro-TRE3G-H2B-mScarlet* was used respectively, in the ratio 1:1. Injections into the cervical spinal cord of P1,P4 or P6 mice were performed using a Hamilton syringe (5 µl) with a mixture of *AAVretro-TRE3G-H2B-mScarlet* and *AAVretro-CAG-DIO-H2B-EGFP* (1:1, 2-2.5 µl) or just *AAVretro-CAG-EGFP* (1-2 µl) as described [99].

Light-Sheet Fluorescence Microscopy

For all anterograde and retrograde injections, post-fixed brains were processed for tissue-clearing, antibody staining and Lightsheet Scanning. A total of 36 brains were processed and imaged by LightSheet Microscopy (by LifeCanvas Technologies (LCT)).

Tissue Preservation, Clearing, Immunolabeling and Imaging

Paraformaldehyde-fixed samples were preserved using SHIELD reagents (LCT) using the manufacturer's instructions [100]. Samples were delipidated using LCT Clear+ delipidation reagents for 2 days. Following delipidation, samples were labeled using eFLASH(Yun et al., 2019) technology which integrates stochastic electrotransport [101] and SWITCH [102], using a SmartBatch+ (or SmartLabel) device (LCT). For immunolabeling, the samples were incubated with 96 µg Chicken anti-GFP, 50 µg Goat anti-RFP, and 72 µg Rabbit NeuN (36 brains) following which the samples were incubated in 50% EasyIndex (RI = 1.52) overnight at 37°C followed by 1 d incubation in 100% EasyIndex for refractive index matching (RI = 1.52). After index matching the samples were imaged using a SmartSPIM axially swept light sheet microscope using a 3.6x objective (0.2 NA) with 4 um z-step, and 1.8 um x-y pixel size.

Atlas Registration (NeuN)

Samples were registered to the Allen Brain Atlas [103] using an automated process (LCT). A NeuN channel for each brain was registered to an average NeuN atlas (generated by using previously registered samples). Registration was performed using successive rigid, affine, and b-spline warping algorithms (SimpleElastix: https://simpleelastix.github.io/).

Cell Detection

Automated cell detection was performed by using a custom convolutional neural network created with the Tensorflow python package (Google, LCT). The cell detection was performed by two networks in sequence. First, a fully- convolutional detection network [104] based on a U-Net architecture [105] was used to find possible positive locations. Second, a convolutional network using a ResNet architecture [106] was used to classify each location as positive or negative. Using the previously calculated Atlas Registration, each cell location was projected onto the Allen Brain Atlas in order to count the number of cells for each atlas- defined region.

Image Segmentation and Thresholding

Process-specific signals were identified by applying an absolute intensity threshold to each voxel within the volumetric image. Voxels exhibiting fluorescence intensity greater than the predetermined threshold were classified as “positive.”

Atlas Registration (Anterograde projections)

The pixels from the resulting segmentation mask were spatially transformed (warped) to the Allen Brain Atlas to determine which region each positive pixel belongs to.

Computation of Fraction Occupation and Percent Occupation

For each anatomical region defined by the registered atlas, the number of positive voxels (i.e., those exceeding the intensity threshold) was summed. This count was then divided by the total voxel count of the same region to yield the fraction occupation metric:

$$\text{Fraction Occupation}_{\text{region}} = \frac{N_{\text{positive voxels, region}}}{N_{\text{total voxels, region}}}$$

$$\text{Percent Occupation}_{\text{region}} = 100 \times \text{Fraction Occupation}_{\text{region}}$$

Coronal Video Reconstruction

Whole Brains were imaged by LightSheet Microscopy horizontally at a resolution of 1.8, 1.8, and 4 um for the medial-lateral, anterior-posterior, and dorsal-ventral axes respectively. The acquired whole-brain image data was resampled to generate a series of raw coronal images with a resolution of 1.8 and 4 um for the medial-lateral and dorsal-ventral axes respectively. The dorsal-ventral axis was downsampled to a resolution of 54 um. To make the video of coronal images, we further downsampled each raw coronal image five times. The display range of each color channel was carefully adjusted linearly to reveal axons and cell bodies of anterograde and retrograde tracing data respectively.

Confocal Microscopy

Confocal photomicrographs were obtained using a Zeiss Laser scanning microscope (LSM 900, in house). Tile-scans were taken with a 5x objective while Z-stacks of optical sections were obtained using either a 10x or a 20x objective. Projection images and illustrations were processed/prepared by Zeiss ZEN software, ImageJ and Adobe Illustrator CC. Various sections of interest from a total of 40 mouse brains were analyzed using confocal microscopy.

Data Analysis

Heatmap Visualization of Projection Patterns

For anterograde projections, fraction occupation percentage data (obtained from the LightSheet analysis pipeline, LCT) were extracted for selected ipsilateral and contralateral brain regions for each injection site. For each injection site, the downstream areas selected across the brain were based on comparisons of equivalent injections (based on coordinates) in the isocortex from the Allen Mouse Brain Connectivity dataset (https://community.brain-map.org/t/api-allen-brain-connectivity/2988). The downstream areas selected for each injection site are listed in Table S1. The data were then normalized, and the mean GFP and RFP values were calculated for each region. For global normalization, Min-Max scaling was applied to the combined GFP and RFP data across both ipsilateral and contralateral regions. The final normalized data were saved for further analysis. Normalized mean fraction occupation for ET^d and ET^i were

visualized as heatmaps, for both ipsilateral and contralateral projections across different selected regions. Region names were aligned along the y-axis, and color intensity scaled to reflect normalized fraction occupation.

Linear Regression and Visualization

ET^d and ET^i fraction occupations for each injection site from target structures of interest (eg: thalamus, midbrain, PONS, medulla were extracted for both ipsilateral and contralateral regions. Structures selected for each of the target structures considered for each injection site are listed in Table S1. For each target structure, linear regression (polyfit) was performed between ET^d and ET^i fraction occupation values. Regression lines were plotted alongside scatter plots of individual data points representing ipsilateral and contralateral areas within each region group. Anatomical area labels were overlaid on the plots using text annotations. ET^d and ET^i fraction occupation values for two region groups compared were normalized using z-score transformation. The z-score for each data point was calculated using the formula:

$$z = (x - \mu) / \sigma$$

where x is the data point, μ is the global mean of the two region groups, and σ is the global standard deviation of two region groups. Percent occupation differences ($\Delta = ET^d - ET^i$) were computed for each target structure. Statistical tests were performed within-group and visualized through boxplots with median, interquartile range, and individual data points along with p-value annotations to indicate statistical significance. To further assess whether the percent occupation differences ($\Delta = ET^d - ET^i$) were uniform across different target structures from an injection site, a multicomparisons test followed by post-hoc comparisons were performed. Post-hoc comparisons were done between different target structures and the thalamus. Since the thalamus in general received significant ET^d and ET^i projections, it was used as a control for comparison with other target structures.

Cell Count Quantification Using Cellpose

Cell body segmentation and quantification for confocal images were performed using the Cellpose algorithm [107], a deep learning-based tool for cellular segmentation. Images were preprocessed for contrast enhancement and background subtraction before input into Cellpose. The “cyto” model was used with default parameters, and the estimated cell diameter was manually specified or automatically determined, depending on image resolution.

Batch segmentation was conducted via the Cellpose GUI or command-line interface, and outputs were visually inspected for accuracy. Resulting masks were used to quantify total cell counts per region or image.

Correlation Analysis

Correlation analysis was performed on either projection fraction occupation values or cell counts across brain regions, on brains scanned by Lightsheet Microscopy. For each subject, direct and indirect data from both hemispheres were combined. Correlation matrices were computed using Pearson correlation coefficients and visualized as heatmaps to compare projection/cell count similarities across individual mice.

Statistical analysis

For statistical comparisons, normality of the dataset was assessed using either the Shapiro-Wilk test or the Kolmogorov-Smirnov test. When data were not normally distributed, non-parametric statistical tests

were used. For multiple comparisons, normality was assessed using the Lilliefors test followed by a nonparametric Kruskal-Wallis test. Post-hoc comparisons of different target regions with thalamus were performed by pairwise Wilcoxon rank-sum tests or Kolmogorov-Smirnov (KS) tests. To control for multiple comparisons while preserving statistical power, all post hoc p-values were corrected using the Benjamini-Hochberg false discovery rate (FDR) method. Significance levels used in the analyses and figures were as follows: *P < 0.05, **P < 0.01, ***P < 0.005, ****P < 0.001, *****P < 0.0001, and n.s. (not significant). Data are presented as median with the 25th–75th percentiles (IQR), or as mean ± s.d., unless otherwise indicated. All statistics were implemented in MATLAB.

Data availability/Code availability

The data that support the findings of this study are available from the lead contact upon reasonable request. Custom-written scripts used in this study are available from: https://github.com/ShreyasDuke/ETd-ETi-Code.git. Anterograde projection and cell distribution video datasets can be viewed at: https://figshare.com/s/4aa9d712da9756bc7551.

REFERENCES:

1. Suryanarayana, S.M., Robertson, B., and Grillner, S. (2022). The neural bases of vertebrate motor behaviour through the lens of evolution. Philos. Trans. R. Soc. Lond. B Biol. Sci. *377*, 20200521.

2. Swanson, L.W. (2000). Cerebral hemisphere regulation of motivated behavior. Brain Res. *886*, 113–164.

3. Douglas, R.J., and Martin, K.A. (2012). Behavioral architecture of the cortical sheet. Curr. Biol. *22*, R1033–R1038.

4. Rakic, P. (2009). Evolution of the neocortex: a perspective from developmental biology. Nat. Rev. Neurosci. *10*, 724–735.

5. Tasic, B., Yao, Z., Graybuck, L.T., Smith, K.A., Nguyen, T.N., Bertagnolli, D., Goldy, J., Garren, E., Economo, M.N., Viswanathan, S., et al. (2018). Shared and distinct transcriptomic cell types across neocortical areas. Nature *563*, 72–78.

6. Harris, K.D., and Shepherd, G.M.G. (2015). The neocortical circuit: themes and variations. Nat. Neurosci. *18*, 170–181.

7. Huang, Z.J. (2014). Toward a genetic dissection of cortical circuits in the mouse. Neuron *83*, 1284–1302.

8. Lemon, R.N., and Griffiths, J. (2005). Comparing the function of the corticospinal system in different species: organizational differences for motor specialization? Muscle Nerve *32*, 261–279.

9. Lemon, R.N. (2008). Descending pathways in motor control. Annu. Rev. Neurosci. *31*, 195–218.

10. Munoz-Castaneda, R., Zingg, B., Matho, K.S., Chen, X., Wang, Q., Foster, N.N., Li, A., Narasimhan, A., Hirokawa, K.E., Huo, B., et al. (2021). Cellular anatomy of the mouse primary motor cortex. Nature *598*, 159–166.

11. Carmona, L.M., Thomas, E.D., Smith, K., Tasic, B., Costa, R.M., and Nelson, A. (2024). Topographical and cell type-specific connectivity of rostral and caudal forelimb corticospinal neuron populations. Cell Rep. *43*, 113993.

12. Economo, M.N., Viswanathan, S., Tasic, B., Bas, E., Winnubst, J., Menon, V., Graybuck, L.T., Nguyen, T.N., Smith, K.A., Yao, Z., et al. (2018). Distinct descending motor cortex pathways and their roles in movement. Nature *563*, 79–84.

13. Shepherd, G.M.G. (2014). Diversity and complexity in the pyramidal tract projectome. Nat. Rev. Neurosci. *15*, 63.

14. Smith, Y., Wichmann, T., and DeLong, M.R. (2014). Corticostriatal and mesocortical dopamine systems: do species differences matter? Nat. Rev. Neurosci. *15*, 63.

15. Kita, T., and Kita, H. (2012). The subthalamic nucleus is one of multiple innervation sites for long-range corticofugal axons: a single-axon tracing study in the rat. J. Neurosci. *32*, 5990–5999.

16. Beattie, R., and Hippenmeyer, S. (2017). Mechanisms of radial glia progenitor cell lineage progression. FEBS Lett. *591*, 3993–4008.

17. Huilgol, D., Levine, J.M., Galbavy, W., Wang, B.S., He, M., Suryanarayana, S.M., and Huang, Z.J. (2023). Direct and indirect neurogenesis generate a mosaic of distinct glutamatergic projection neuron types in cerebral cortex. Neuron. https://doi.org/10.1016/j.neuron.2023.05.021.

18. Martinez-Cerdeno, V., Noctor, S.C., and Kriegstein, A.R. (2006). The role of intermediate progenitor cells in the evolutionary expansion of the cerebral cortex. Cereb. Cortex *16 Suppl 1*, i152–i161.

19. Noctor, S.C., Martinez-Cerdeno, V., Ivic, L., and Kriegstein, A.R. (2004). Cortical neurons arise in symmetric and asymmetric division zones and migrate through specific phases. Nat. Neurosci. *7*, 136–144.

20. Kriegstein, A., Noctor, S., and Martínez-Cerdeño, V. (2006). Patterns of neural stem and progenitor cell division may underlie evolutionary cortical expansion. Nat. Rev. Neurosci. *7*, 883–890.

21. Kriegstein, A., and Alvarez-Buylla, A. (2009). The glial nature of embryonic and adult neural stem cells. Annu. Rev. Neurosci. *32*, 149–184.

22. Dimou, L., and Götz, M. (2014). Glial cells as progenitors and stem cells: new roles in the healthy and diseased brain. Physiol. Rev. *94*, 709–737.

23. Hevner, R.F. (2019). Intermediate progenitors and Tbr2 in cortical development. J. Anat. *235*, 616–625.

24. Florio, M., and Huttner, W.B. (2014). Neural progenitors, neurogenesis and the evolution of the neocortex. Development *141*, 2182–2194.

25. Baumann, N., Wagener, R.J., Javed, A., Conti, E., Abe, P., Lopes, A., Sansevrino, R., Lavalley, A., Magrinelli, E., Szalai, T., et al. (2025). Regional differences in progenitor metabolism shape brain growth during development. Cell. https://doi.org/10.1016/j.cell.2025.04.003.

26. Quintana-Urzainqui, I., Oel, P.A., Gerber, T., Pan, L., Papadopoulos, N., Serka, Z.G., Verbanac, A., Börsig, M., Torres-Sabino, D., Rollán-Delgado, I.C., et al. (2025). Developmental landscape of shark telencephalon sheds light on the evolution of telencephalic cell types and the ancient origin of Cajal-Retzius cells. bioRxiv. https://doi.org/10.1101/2025.05.08.652169.

27. Cárdenas, A., and Borrell, V. (2020). Molecular and cellular evolution of corticogenesis in amniotes. Cell. Mol. Life Sci. *77*, 1435–1460.

28. Espinós, A., Fernández-Ortuño, E., Negri, E., and Borrell, V. (2022). Evolution of genetic mechanisms regulating cortical neurogenesis. Dev. Neurobiol. *82*, 428–453.

29. Hatanaka, Y., Yamada, K., Eritate, T., Kawaguchi, Y., and Hirata, T. (2024). Neuronal fate resulting from indirect neurogenesis in the mouse neocortex. Cereb. Cortex *34*. https://doi.org/10.1093/cercor/bhae439.

30. An, X., Matho, K.S., Li, Y., Mohan, H., Xu, X.H., Whisaw, I., Kepecs, A., and Huang, J. (2022). A cortical circuit for orchestrating oromanual food manipulation. bioRxiv. https://doi.org/10.1101/2022.12.03.518964.

31. Brown, A.R., and Teskey, G.C. (2014). Motor cortex is functionally organized as a set of spatially distinct representations for complex movements. J. Neurosci. *34*, 13574–13585.

32. Morandell, K., and Huber, D. (2017). The role of forelimb motor cortex areas in goal directed action in mice. Sci. Rep. *7*, 15759.

33. Tennant, K.A., Adkins, D.L., Donlan, N.A., Asay, A.L., Thomas, N., Kleim, J.A., and Jones, T.A. (2011). The organization of the forelimb representation of the C57BL/6 mouse motor cortex as defined by intracortical microstimulation and cytoarchitecture. Cereb. Cortex *21*, 865–876.

34. Li, Y., An, X., Mulcahey, P.J., Qian, Y., Xu, X.H., Zhao, S., Mohan, H., Suryanarayana, S.M., Bachschmid-Romano, L., Brunel, N., et al. (2024). Cortico-thalamic communication for action coordination in a skilled motor sequence. bioRxiv, 2023.10.25.563871.

35. Grillner, S., Robertson, B., and Kotaleski, J.H. (2020). Basal Ganglia-A Motion Perspective. Compr. Physiol. *10*, 1241–1275.

36. Markowitz, J.E., Gillis, W.F., Beron, C.C., Neufeld, S.Q., Robertson, K., Bhagat, N.D., Peterson, R.E., Peterson, E., Hyun, M., Linderman, S.W., et al. (2018). The Striatum Organizes 3D Behavior via Moment-to-Moment Action Selection. Cell *174*, 44–58 e17.

37. Sherman, S.M., and Guillery, R.W. (2001). Exploring the thalamus (Elsevier).

38. Mohan, H., An, X., Xu, X.H., Kondo, H., Zhao, S., Matho, K.S., Wang, B.S., Musall, S., Mitra, P., and Huang, Z.J. (2023). Cortical glutamatergic projection neuron types contribute to distinct functional subnetworks. Nat. Neurosci. *26*, 481–494.

39. Binkofski, F., and Buccino, G. (2018). The role of the parietal cortex in sensorimotor transformations and action coding. Handb. Clin. Neurol. *151*, 467–479.

40. Anastasiades, P.G., and Carter, A.G. (2021). Circuit organization of the rodent medial prefrontal cortex. Trends Neurosci. *44*, 550–563.

41. Riccomagno, M.M., and Kolodkin, A.L. (2015). Sculpting neural circuits by axon and dendrite pruning. Annu. Rev. Cell Dev. Biol. *31*, 779–805.

42. Luo, L., and O'Leary, D.D.M. (2005). Axon retraction and degeneration in development and disease. Annu. Rev. Neurosci. *28*, 127–156.

43. Stanfield, B.B., O'Leary, D.D., and Fricks, C. (1982). Selective collateral elimination in early postnatal development restricts cortical distribution of rat pyramidal tract neurones. Nature *298*, 371–373.

44. Abe, P., Lavalley, A., Morassut, I., Santinha, A.J., Roig-Puiggros, S., Javed, A., Klingler, E., Baumann, N., Prados, J., Platt, R.J., et al. (2024). Molecular programs guiding arealization of descending cortical pathways. Nature *634*, 644–651.

45. Lemon, R. (2019). Recent advances in our understanding of the primate corticospinal system. F1000Res. *8*. https://doi.org/10.12688/f1000research.17445.1.

46. Brain Initiative Cell Census Network (2021). A multimodal cell census and atlas of the mammalian primary motor cortex. Nature *598*, 86–102.

47. Ocana, F.M., Suryanarayana, S.M., Saitoh, K., Kardamakis, A.A., Capantini, L., Robertson, B., and Grillner, S. (2015). The lamprey pallium provides a blueprint of the mammalian motor projections from cortex. Curr. Biol. *25*, 413–423.

48. Suryanarayana, S.M., Robertson, B., Wallen, P., and Grillner, S. (2017). The Lamprey Pallium Provides a Blueprint of the Mammalian Layered Cortex. Curr. Biol. *27*, 3264–3277 e5.

49. Suryanarayana, S.M., Perez-Fernandez, J., Robertson, B., and Grillner, S. (2022). The Lamprey Forebrain - Evolutionary Implications. Brain Behav. Evol. *96*, 318–333.

50. Lopes, G., and Kampff, A.R. (2015). Cortical control: learning from the lamprey. Curr. Biol. *25*, R203–R205.

51. Isa, T., Marquez-Legorreta, E., Grillner, S., and Scott, E.K. (2021). The tectum/superior colliculus as the vertebrate solution for spatial sensory integration and action. Curr. Biol. *31*, R741–R762.

52. Grillner, S., and Robertson, B. (2016). The Basal Ganglia Over 500 Million Years. Curr. Biol. *26*, R1088–r1100.

53. Grillner, S., and El Manira, A. (2020). Current Principles of Motor Control, with Special Reference to Vertebrate Locomotion. Physiol. Rev. *100*, 271–320.

54. Briscoe, S.D., and Ragsdale, C.W. (2019). Evolution of the Chordate Telencephalon. Curr. Biol. *29*, R647–R662.

55. Briscoe, S.D., and Ragsdale, C.W. (2018). Homology, neocortex, and the evolution of developmental mechanisms. Science *362*, 190–193.

56. Ruder, L., and Arber, S. (2019). Brainstem Circuits Controlling Action Diversification. Annu. Rev. Neurosci. *42*, 485–504.

57. Arber, S., and Costa, R.M. (2022). Networking brainstem and basal ganglia circuits for movement. Nat. Rev. Neurosci. *23*, 342–360.

58. Arber, S., and Costa, R.M. (2018). Connecting neuronal circuits for movement. Science *360*, 1403–1404.

59. Arlotta, P., Molyneaux, B.J., Chen, J., Inoue, J., Kominami, R., and Macklis, J.D. (2005). Neuronal subtype-specific genes that control corticospinal motor neuron development in vivo. Neuron *45*, 207–221.

60. Cisek, P. (2022). Evolution of behavioural control from chordates to primates. Philos. Trans. R. Soc. Lond. B Biol. Sci. *377*, 20200522.

61. Suryanarayana, S.M., and Huilgol, D. (2023). Conservation and diversification of pallial cell types across

vertebrates - an evo-devo perspective. Brain Behav. Evol. https://doi.org/10.1159/000531718.

62. Mayrhofer, J.M., El-Boustani, S., Foustoukos, G., Auffret, M., Tamura, K., and Petersen, C.C.H. (2019). Distinct Contributions of Whisker Sensory Cortex and Tongue-Jaw Motor Cortex in a Goal-Directed Sensorimotor Transformation. Neuron *103*, 1034–1043 e5.

63. Yang, W., Kanodia, H., and Arber, S. (2023). Structural and functional map for forelimb movement phases between cortex and medulla. Cell *186*, 162–177 e18.

64. Barthas, F., and Kwan, A.C. (2017). Secondary Motor Cortex: Where "Sensory" Meets "Motor" in the Rodent Frontal Cortex. Trends Neurosci. *40*, 181–193.

65. Wool, L., Lak, A., Carandini, M., and Harris, K. (2023). Mouse frontal cortex nonlinearly encodes stimuli, choices, and outcomes [version 1; peer review: 1 approved, 1 approved with reservations]. Wellcome Open Res. *8*. https://doi.org/10.12688/wellcomeopenres.19693.1.

66. Zatka-Haas, P., Steinmetz, N.A., Carandini, M., and Harris, K.D. (2021). Sensory coding and the causal impact of mouse cortex in a visual decision. Elife *10*. https://doi.org/10.7554/eLife.63163.

67. Ferenczi, E.A., Wang, W., Biswas, A., Pottala, T., Dong, Y., Chan, A.K., Albanese, M.A., Sohur, R.S., Jia, T., Mastro, K.J., et al. (2024). Projections between the globus pallidus externa and cortex span motor and non-motor regions. bioRxiv, 2024.11.08.622712.

68. Thompson, W.S., Grillner, S., and Silberberg, G. (2024). Motor cortex directly excites the output nucleus of the basal ganglia, the substantia nigra pars reticulata. bioRxiv, 2024.03.19.585632.

69. Grillner, S. (2025). How circuits for habits are formed within the basal ganglia. Proc. Natl. Acad. Sci. U. S. A. *122*, e2423068122.

70. Yin, H.H., and Knowlton, B.J. (2006). The role of the basal ganglia in habit formation. Nat. Rev. Neurosci. *7*, 464–476.

71. Kawai, R., Markman, T., Poddar, R., Ko, R., Fantana, A.L., Dhawale, A.K., Kampff, A.R., and Olveczky, B.P. (2015). Motor cortex is required for learning but not for executing a motor skill. Neuron *86*, 800–812.

72. Graybiel, A.M. (2008). Habits, rituals, and the evaluative brain. Annu. Rev. Neurosci. *31*, 359–387.

73. Redgrave, P., Prescott, T.J., and Gurney, K. (1999). The basal ganglia: a vertebrate solution to the selection problem? Neuroscience *89*, 1009–1023.

74. Galazo, M.J., Sweetser, D.A., and Macklis, J.D. (2023). Tle4 controls both developmental acquisition and early post-natal maturation of corticothalamic projection neuron identity. Cell Rep. *42*, 112957.

75. Tsyporin, J., Tastad, D., Ma, X., Nehme, A., Finn, T., Huebner, L., Liu, G., Gallardo, D., Makhamreh, A., Roberts, J.M., et al. (2021). Transcriptional repression by FEZF2 restricts alternative identities of cortical projection neurons. Cell Rep. *35*, 109269.

76. Petersen, C.C. (2007). The functional organization of the barrel cortex. Neuron *56*, 339–355.

77. Kaas, J.H. (2011). Reconstructing the areal organization of the neocortex of the first mammals. Brain Behav. Evol. *78*, 7–21.

78. Kaas, J.H. (2013). The evolution of brains from early mammals to humans. Wiley Interdiscip. Rev. Cogn. Sci. *4*, 33–45.

79. Crombie, D., and Busse, L. (2021). Should I stay or should I go? A thalamic circuit for modulating behavioral responses to visual threat. Neuron *109*, 3717–3719.

80. Fratzl, A., Koltchev, A.M., Vissers, N., Tan, Y.L., Marques-Smith, A., Stempel, A.V., Branco, T., and Hofer, S.B. (2021). Flexible inhibitory control of visually evoked defensive behavior by the ventral lateral geniculate nucleus. Neuron *109*, 3810–3822 e9.

81. Mederos, S., Blakely, P., Vissers, N., Clopath, C., and Hofer, S.B. (2025). Overwriting an instinct: Visual cortex instructs learning to suppress fear responses. Science *387*, 682–688.

82. Veinante, P., and Deschenes, M. (1999). Single- and multi-whisker channels in the ascending projections from the principal trigeminal nucleus in the rat. J. Neurosci. *19*, 5085–5095.

83. Brecht, M., and Sakmann, B. (2002). Whisker maps of neuronal subclasses of the rat ventral posterior medial thalamus, identified by whole-cell voltage recording and morphological reconstruction. J. Physiol. *538*, 495–515.

84. Grothe, B., Pecka, M., and McAlpine, D. (2010). Mechanisms of sound localization in mammals. Physiol. Rev. *90*, 983–1012.

85. Du, X., Xu, H., Song, P., Zhai, Y., Ye, H., Bao, X., Huang, Q., Tanigawa, H., Tu, Z., Chen, P., et al. (2025). The multifaceted role of the inferior colliculus in sensory prediction, reward processing, and decision-making. Elife *13*. https://doi.org/10.7554/eLife.101142.

86. Carandini, M., and Churchland, A.K. (2013). Probing perceptual decisions in rodents. Nat. Neurosci. *16*, 824–831.

87. Odoemene, O., Pisupati, S., Nguyen, H., and Churchland, A.K. (2018). Visual Evidence Accumulation Guides Decision-Making in Unrestrained Mice. J. Neurosci. *38*, 10143–10155.

88. Miller, E.K. (2000). The prefrontal cortex and cognitive control. Nat. Rev. Neurosci. *1*, 59–65.

89. Allsop, S.A., Wichmann, R., Mills, F., Burgos-Robles, A., Chang, C.J., Felix-Ortiz, A.C., Vienne, A., Beyeler, A., Izadmehr, E.M., Glober, G., et al. (2018). Corticoamygdala Transfer of Socially Derived Information Gates Observational Learning. Cell *173*, 1329–1342 e18.

90. Gangopadhyay, P., Chawla, M., Dal Monte, O., and Chang, S.W.C. (2021). Prefrontal-amygdala circuits in social decision-making. Nat. Neurosci. *24*, 5–18.

91. Eichenbaum, H. (2017). Prefrontal-hippocampal interactions in episodic memory. Nat. Rev. Neurosci. *18*, 547–558.

92. Jin, J., and Maren, S. (2015). Prefrontal-Hippocampal Interactions in Memory and Emotion. Front. Syst. Neurosci. *9*, 170.

93. Souza, R., Bueno, D., Lima, L.B., Muchon, M.J., Goncalves, L., Donato, J., Jr, Shammah-Lagnado, S.J., and Metzger, M. (2022). Top-down projections of the prefrontal cortex to the ventral tegmental area, laterodorsal tegmental nucleus, and median raphe nucleus. Brain Struct. Funct. *227*, 2465–2487.

94. Zhong, H., Xu, H., Li, X., Xie, R.G., Shi, Y., Wang, Y., Tong, L., Zhu, Q., Han, J., Tao, H., et al. (2023). A role of prefrontal cortico-hypothalamic projections in wake promotion. Cereb. Cortex *33*, 3026–3042.

95. Buijs, R.M., and Van Eden, C.G. (2000). The integration of stress by the hypothalamus, amygdala and

prefrontal cortex: balance between the autonomic nervous system and the neuroendocrine system. Prog. Brain Res. *126*, 117–132.

96. He, M., Tucciarone, J., Lee, S., Nigro, M.J., Kim, Y., Levine, J.M., Kelly, S.M., Krugikov, I., Wu, P., Chen, Y., et al. (2016). Strategies and tools for combinatorial targeting of GABAergic neurons in mouse cerebral cortex. Neuron *91*, 1228–1243.

97. Matho, K.S., Huilgol, D., Galbavy, W., He, M., Kim, G., An, X., Lu, J., Wu, P., Di Bella, D.J., Shetty, A.S., et al. (2021). Genetic dissection of the glutamatergic neuron system in cerebral cortex. Nature *598*, 182–187.

98. Chaterji, S., Barik, A., and Sathyamurthy, A. (2021). Intraspinal injection of adeno-associated viruses into the adult mouse spinal cord. STAR Protoc. *2*, 100786.

99. Ayers, J.I., Fromholt, S., Sinyavskaya, O., Siemienski, Z., Rosario, A.M., Li, A., Crosby, K.W., Cruz, P.E., DiNunno, N.M., Janus, C., et al. (2015). Widespread and efficient transduction of spinal cord and brain following neonatal AAV injection and potential disease modifying effect in ALS mice. Mol. Ther. *23*, 53–62.

100. Park, Y.G., Sohn, C.H., Chen, R., McCue, M., Yun, D.H., Drummond, G.T., Ku, T., Evans, N.B., Oak, H.C., Trieu, W., et al. (2018). Protection of tissue physicochemical properties using polyfunctional crosslinkers. Nat. Biotechnol. https://doi.org/10.1038/nbt.4281.

101. Kim, S.Y., Cho, J.H., Murray, E., Bakh, N., Choi, H., Ohn, K., Ruelas, L., Hubbert, A., McCue, M., Vassallo, S.L., et al. (2015). Stochastic electrotransport selectively enhances the transport of highly electromobile molecules. Proc. Natl. Acad. Sci. U. S. A. *112*, E6274–E6283.

102. Murray, E., Cho, J.H., Goodwin, D., Ku, T., Swaney, J., Kim, S.Y., Choi, H., Park, Y.G., Park, J.Y., Hubbert, A., et al. (2015). Simple, Scalable Proteomic Imaging for High-Dimensional Profiling of Intact Systems. Cell *163*, 1500–1514.

103. Wang, Q., Ding, S.L., Li, Y., Royall, J., Feng, D., Lesnar, P., Graddis, N., Naeemi, M., Facer, B., Ho, A., et al. (2020). The Allen Mouse Brain Common Coordinate Framework: A 3D Reference Atlas. Cell *181*, 936–953 e20.

104. Shelhamer, E., Long, J., and Darrell, T. (2016). Fully convolutional networks for semantic segmentation. IEEE Trans. Pattern Anal. Mach. Intell. *39*, 640–651.

105. Ronneberger, O., Fischer, P., and Brox, T. (2015). U-net: Convolutional networks for biomedical image segmentation (Springer).

106. He, K., Zhang, X., Ren, S., and Sun, J. (2016). Deep residual learning for image recognition.

107. Stringer, C., Wang, T., Michaelos, M., and Pachitariu, M. (2021). Cellpose: a generalist algorithm for cellular segmentation. Nat. Methods *18*, 100–106.

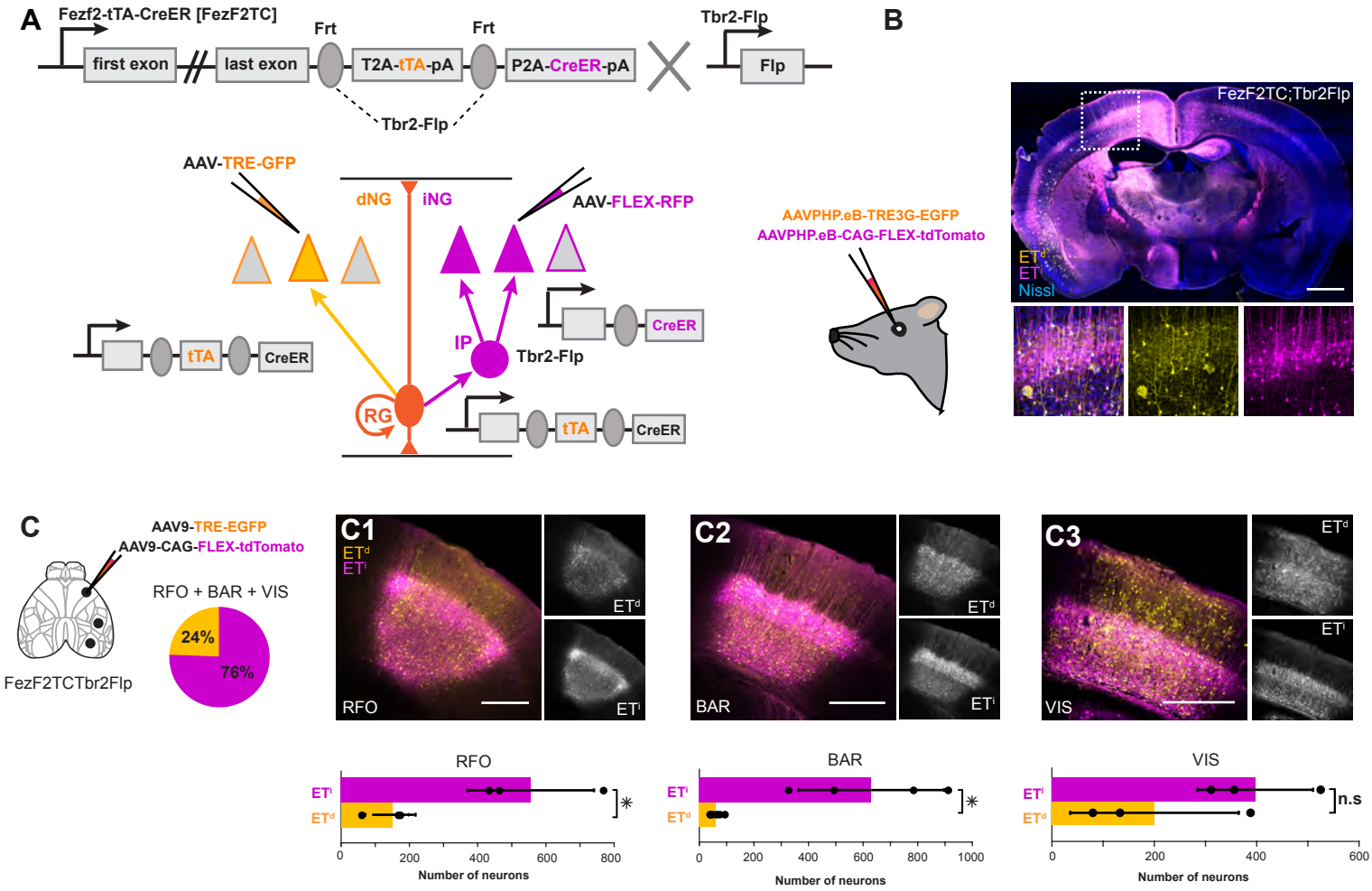
A
Fezf2-tTA-CreER [FezF2TC]
first exon
last exon
Frt
Frt
T2A-tTA-pA
P2A-CreER-pA
Tbr2-Flp
Tbr2-Flp
Flp
B
AAV-TRE-GFP
dNG
iNG
AAV-FLEX-RFP
tTA
CreER
IP
Tbr2-Flp
CreER
RG
tTA
CreER
AAVPHP.eB-TRE3G-EGFP
AAVPHP.eB-CAG-FLEX-tdTomato
FezF2TC;Tbr2Flp
ETd
ETi
Nissl
C
AAV9-TRE-EGFP
AAV9-CAG-FLEX-tdTomato
FezF2TCTbr2Flp
RFO + BAR + VIS
24%
76%
C1
ETd
ETi
RFO
ETd
ETi
C2
BAR
ETd
ETi
C3
VIS
ETd
ETi
RFO
ETi
ETd
*
0
200
400
600
800
Number of neurons
BAR
ETi
ETd
*
0
200
400
600
800
1000
Number of neurons
VIS
ETi
ETd
n.s
0
200
400
600
Number of neurons

Figure1

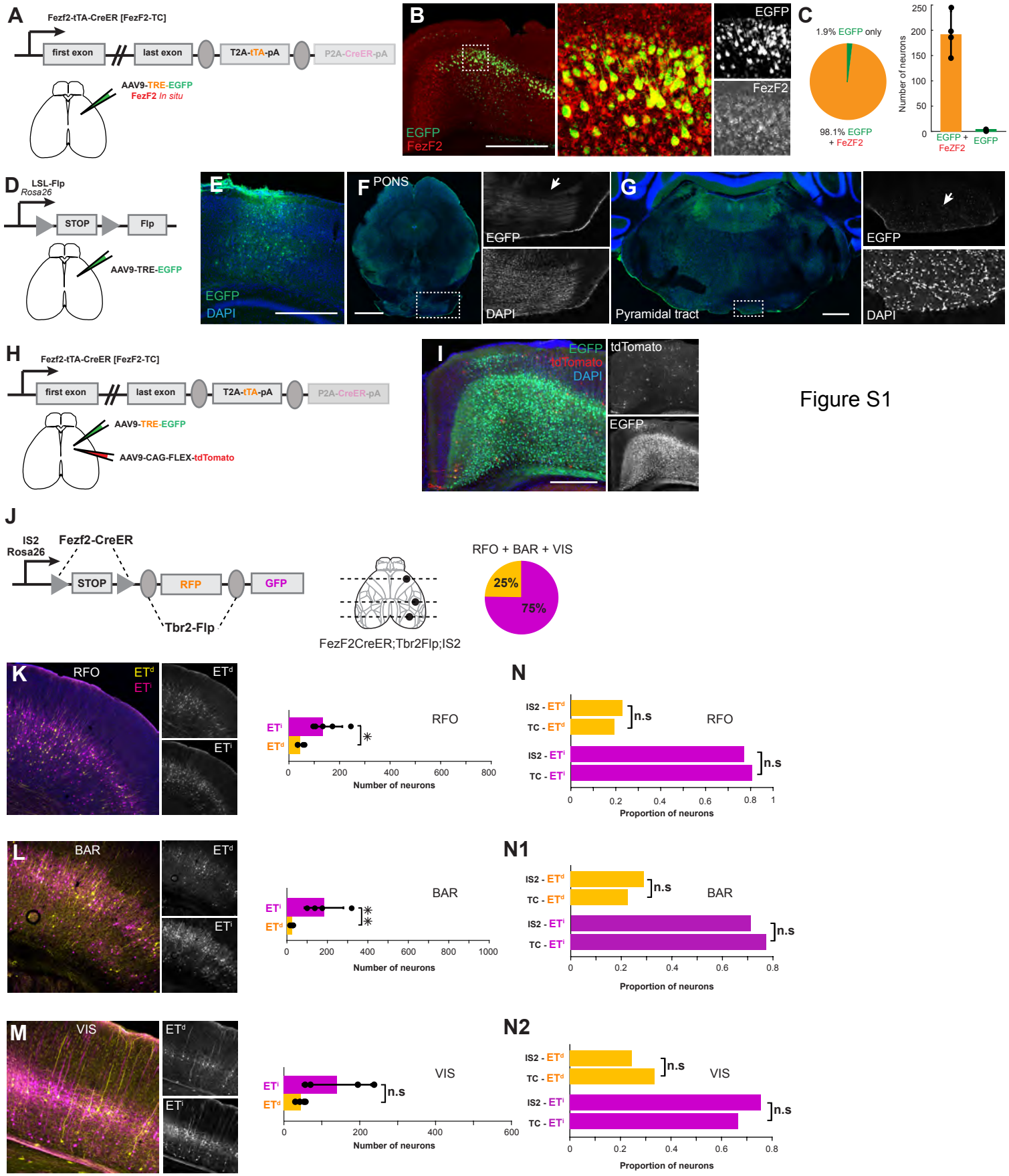

Figure S1

Figure S1, Related to Figure 1

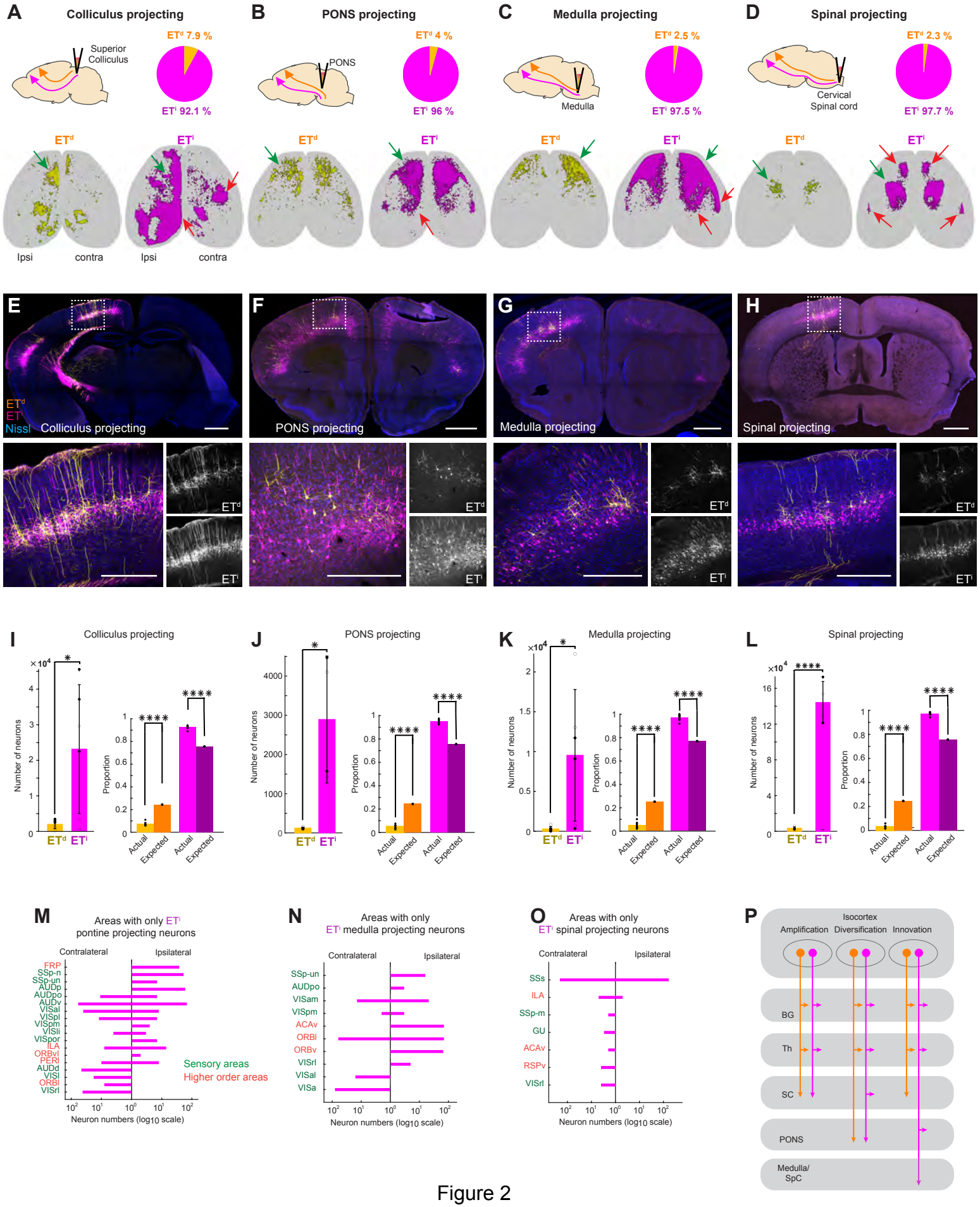
A
Colliculus projecting
Superior Colliculus
ETd 7.9 %
ETi 92.1 %
B
PONS projecting
PONS
ETd 4 %
ETi 96 %
C
Medulla projecting
Medulla
ETd 2.5 %
ETi 97.5 %
D
Spinal projecting
Cervical Spinal cord
ETd 2.3 %
ETi 97.7 %
ETd
ETi
Ipsi
contra
E
F
G
H
Nissl
Colliculus projecting
PONS projecting
Medulla projecting
Spinal projecting
I
J
K
L
Number of neurons
Proportion
Actual
Expected
M
Areas with only ETi pontine projecting neurons
Contralateral
Ipsilateral
FRP
SSp-n
SSp-un
AUDp
AUDpo
AUDv
VISal
VISpl
VISpm
VISli
VISpor
ILA
ORBvl
PERI
AUDd
VISl
ORBl
VISrl
Sensory areas
Higher order areas
Neuron numbers (log10 scale)
N
Areas with only ETi medulla projecting neurons
SSp-un
AUDpo
VISam
VISpm
ACAv
ORBl
ORBv
VISrl
VISal
VISa
O
Areas with only ETi spinal projecting neurons
SSs
ILA
SSp-m
GU
ACAv
RSPv
VISrl
P
Isocortex
Amplification
Diversification
Innovation
BG
Th
SC
PONS
Medulla/ SpC

Figure 2

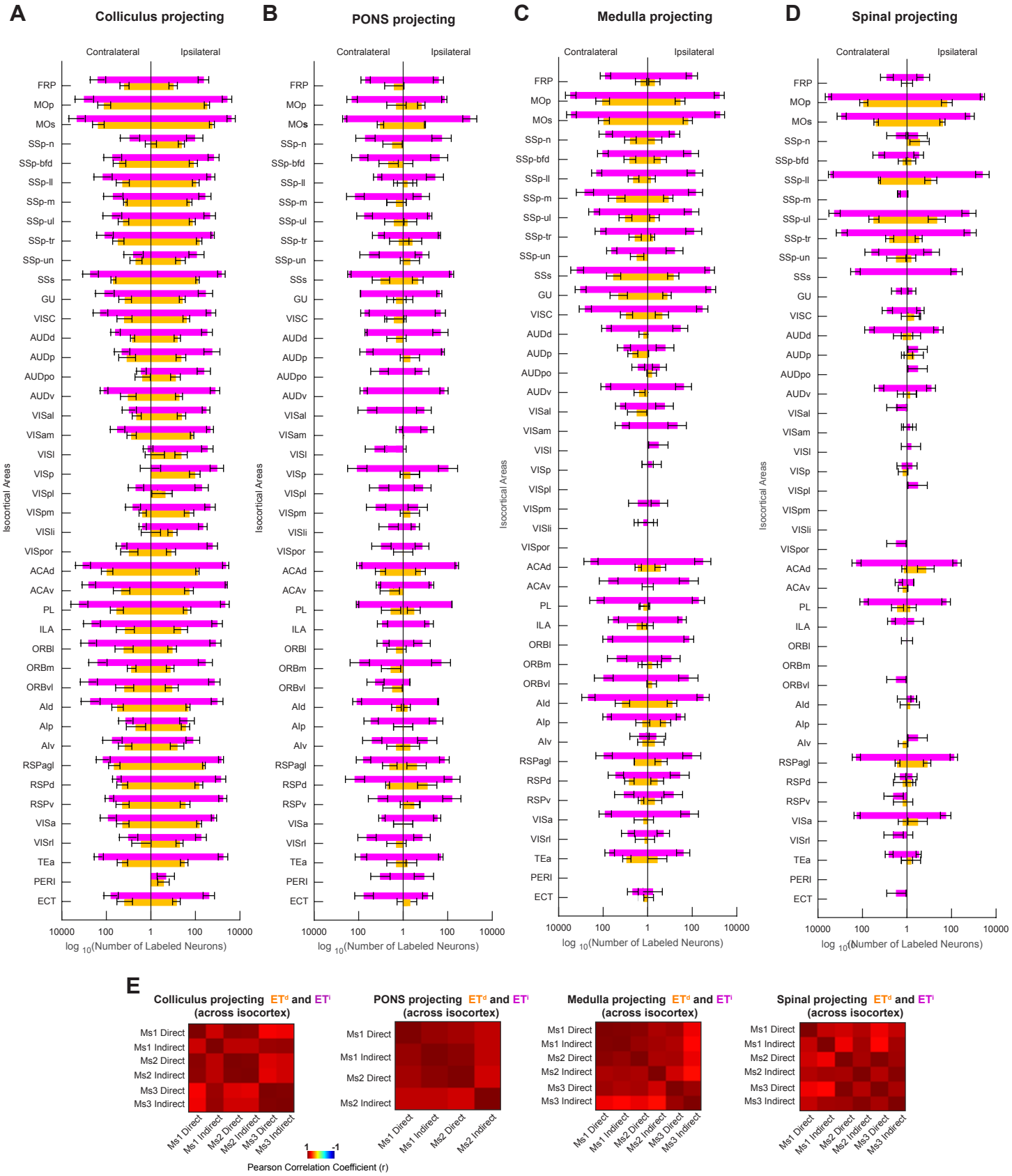

Figure S2, Related to FIgure 2

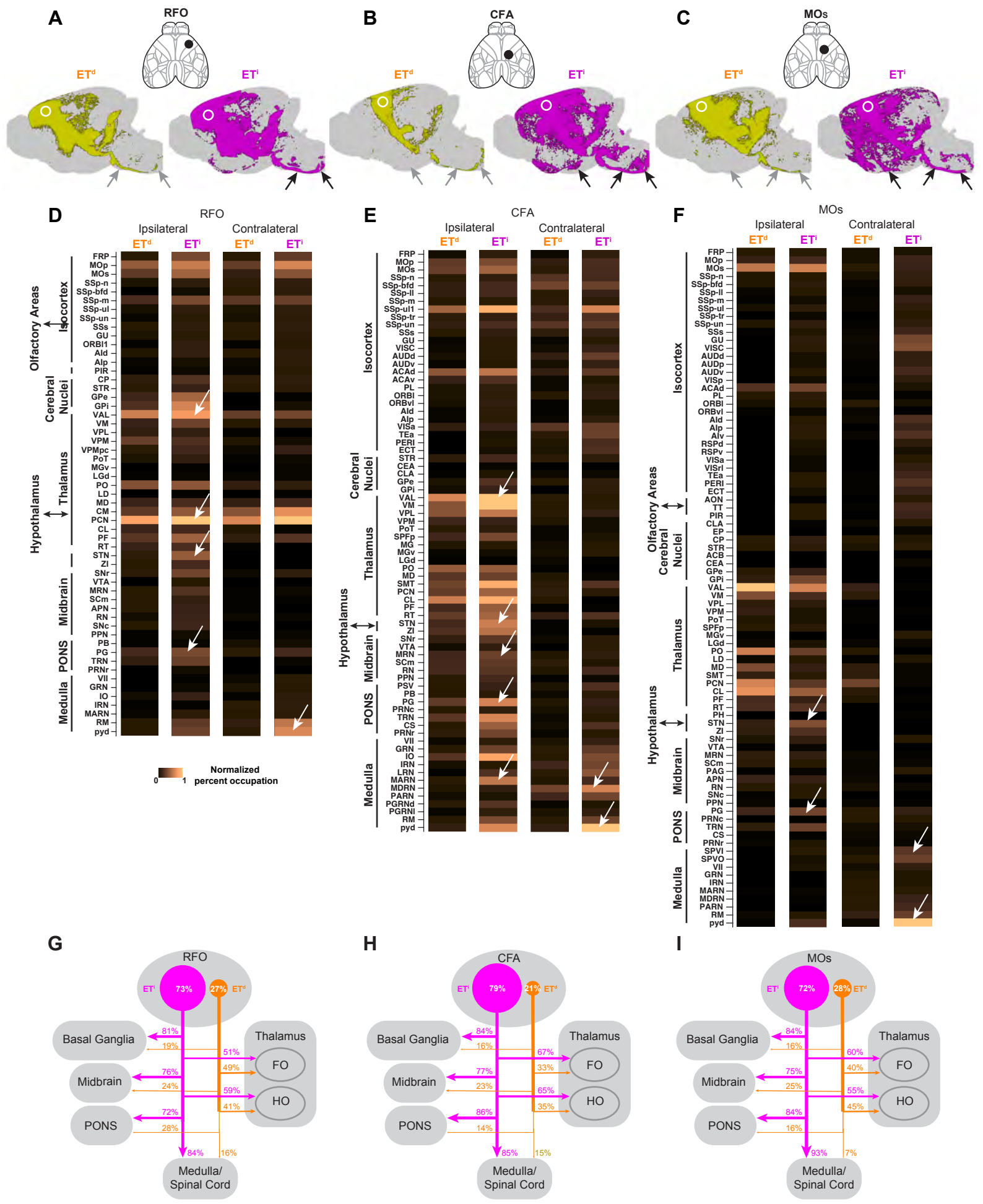
A
RFO
ET^d
ET^i
B
CFA
C
MOs
D
RFO
Ipsilateral
Contralateral
Olfactory Areas
Isocortex
Cerebral Nuclei
Hypothalamus
Thalamus
Midbrain
PONS
Medulla
Normalized percent occupation
E
CFA
F
MOs
G
RFO
73%
27%
Basal Ganglia
Thalamus
Midbrain
PONS
FO
HO
Medulla/ Spinal Cord
H
CFA
79%
21%
I
MOs
72%
28%

Figure 3

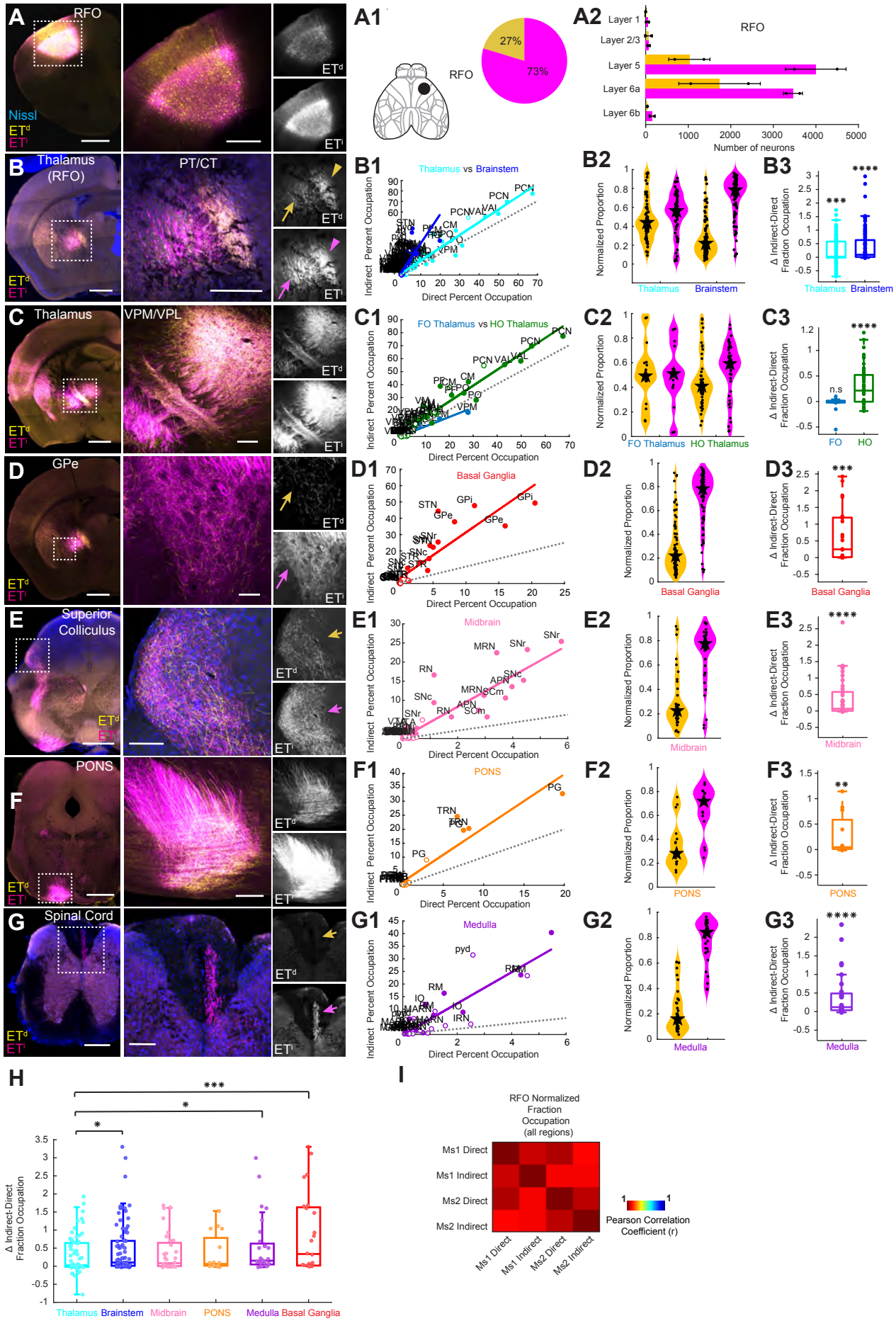

Figure S3, Related to Figure 3

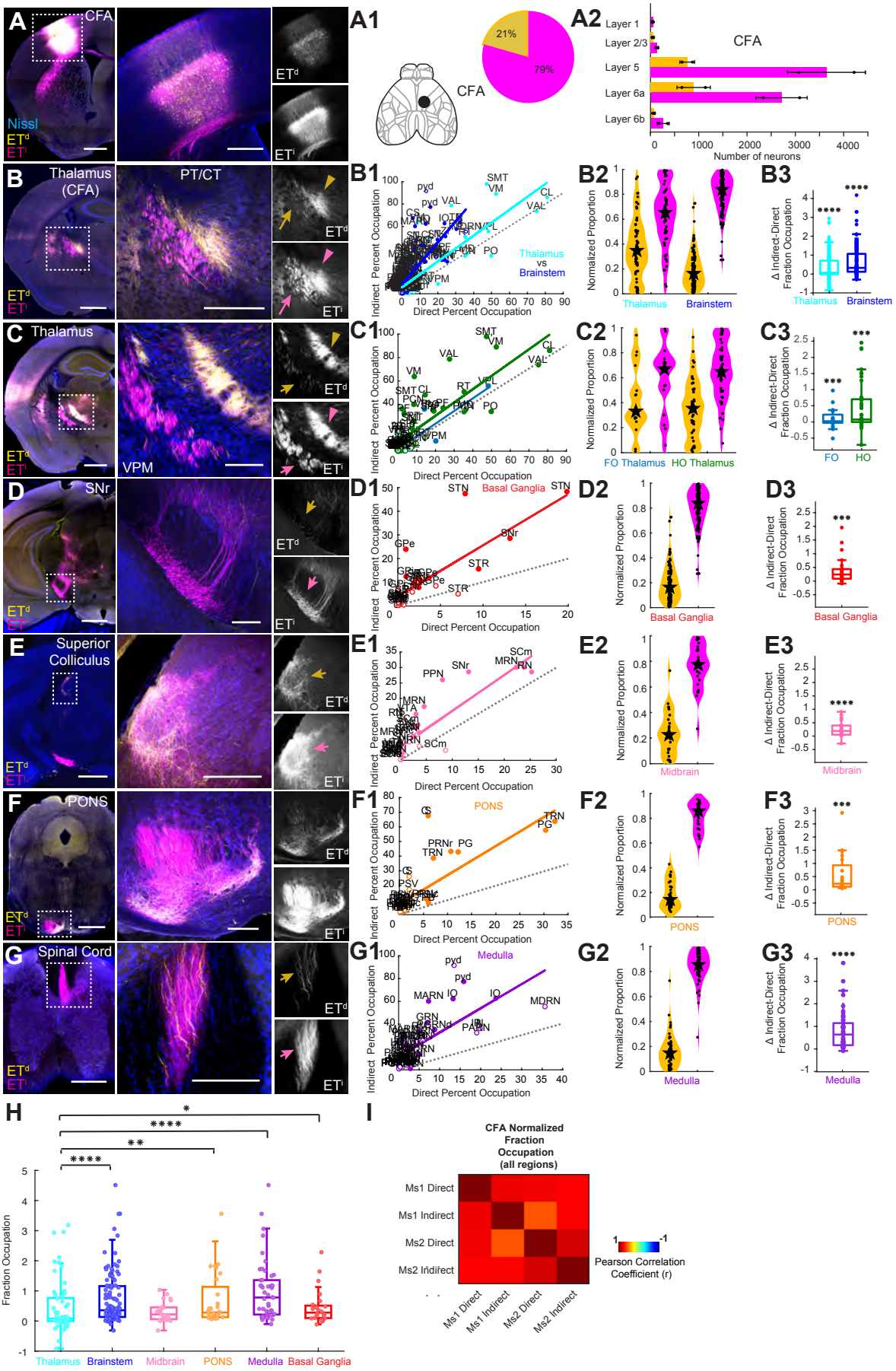

Figure S4, Related to Figure 3

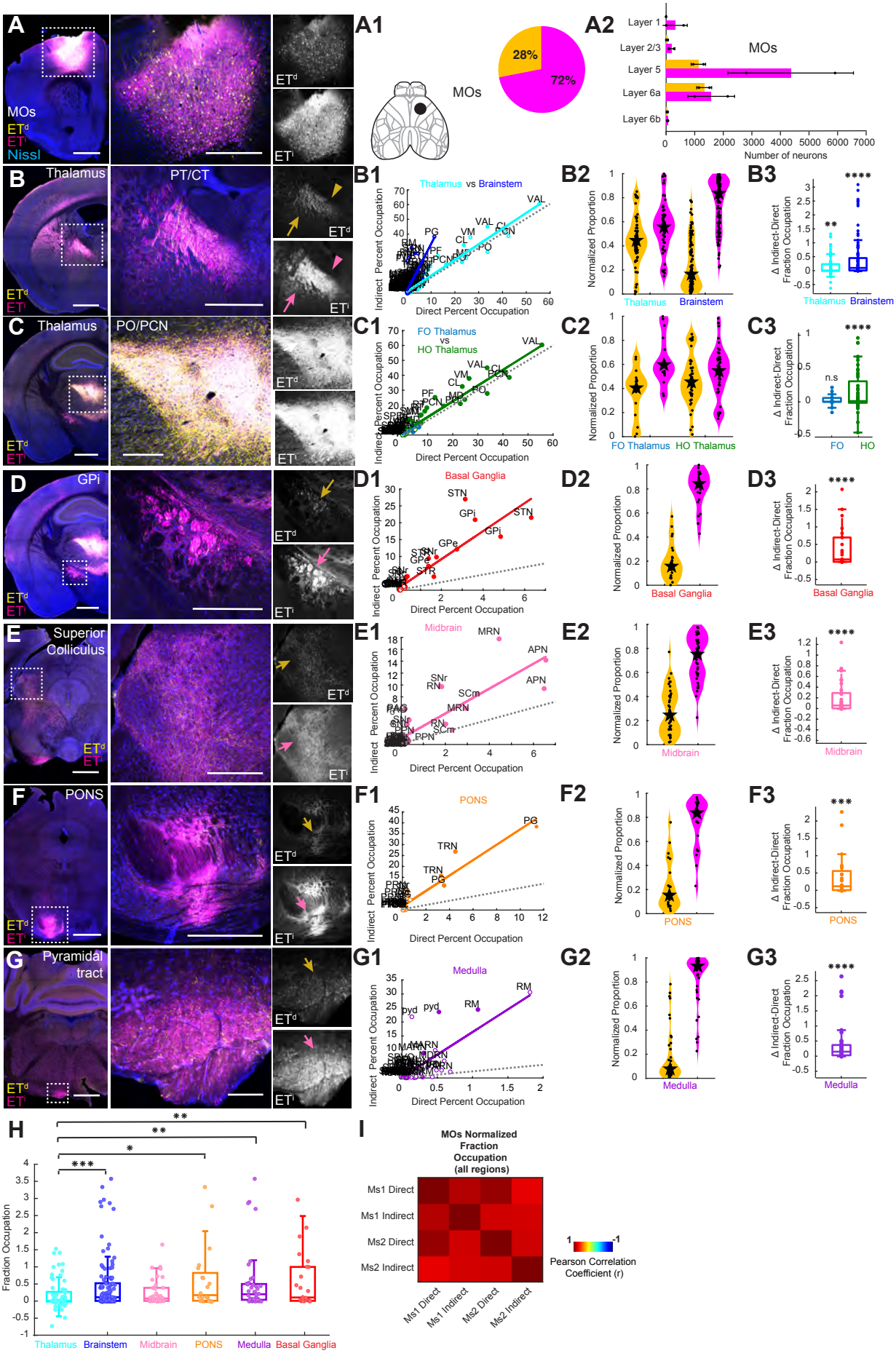

Figure S5, Related to Figure 3

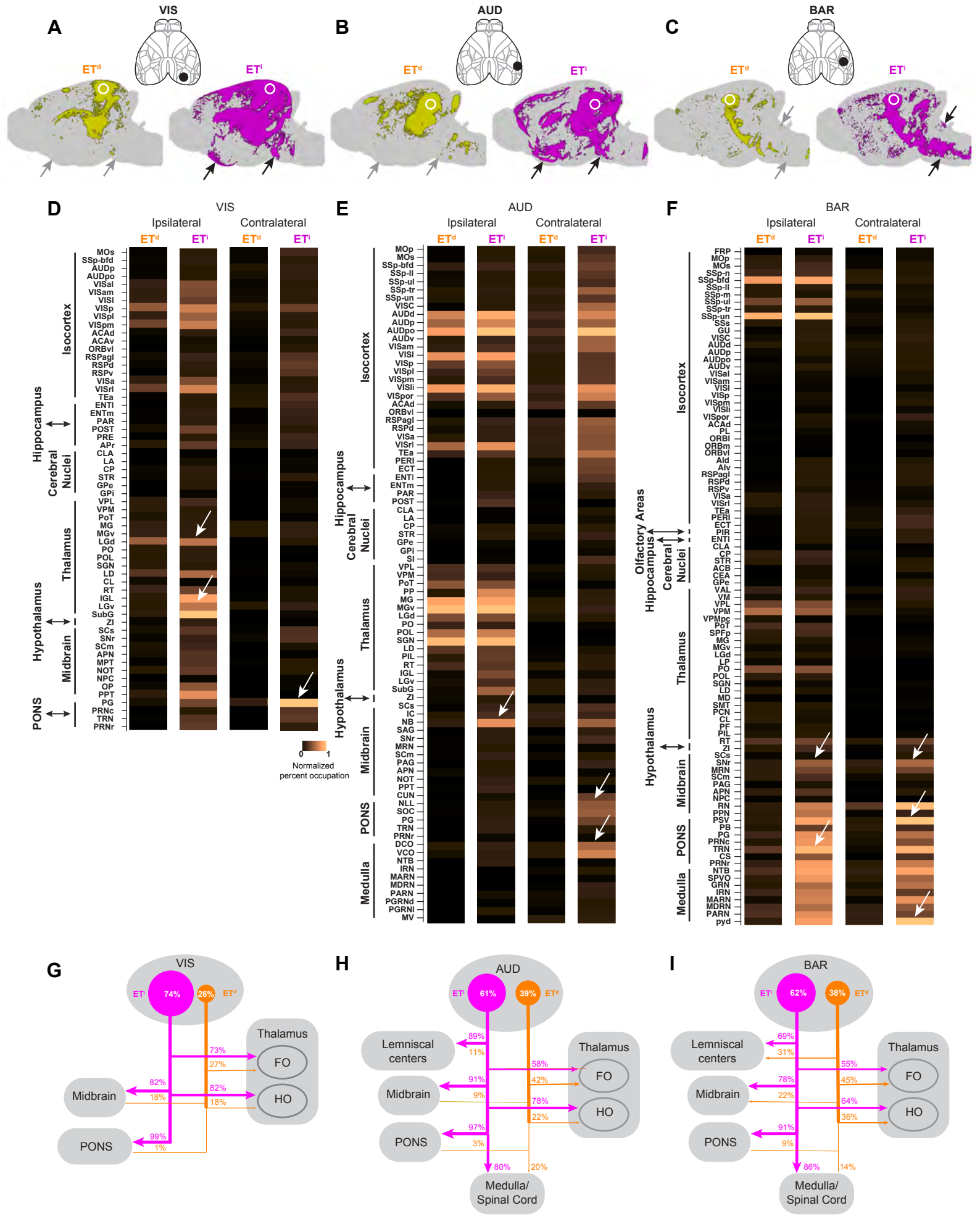
A
VIS
ETd
ETi
B
AUD
ETd
ETi
C
BAR
ETd
ETi
D
VIS
Ipsilateral
Contralateral
ETd
ETi
ETd
ETi
Isocortex
Hippocampus
Cerebral Nuclei
Thalamus
Hypothalamus
Midbrain
PONS
MOs
SSp-bfd
AUDp
AUDpo
VISal
VISam
VISl
VISp
VISpl
VISpm
ACAd
ACAv
ORBvl
RSPagl
RSPd
RSPv
VISa
VISrl
TEa
ENTl
ENTm
PAR
POST
PRE
APr
CLA
LA
CP
STR
GPe
GPi
VPL
VPM
PoT
MG
MGv
LGd
PO
POL
SGN
LD
CL
RT
IGL
LGv
SubG
ZI
SCs
SNr
SCm
APN
MPT
NOT
NPC
OP
PPT
PG
PRNc
TRN
PRNr
0
1
Normalized percent occupation
E
AUD
Ipsilateral
Contralateral
ETd
ETi
ETd
ETi
Isocortex
Hippocampus
Cerebral Nuclei
Thalamus
Hypothalamus
Midbrain
PONS
Medulla
MOp
MOs
SSp-bfd
SSp-ll
SSp-ul
SSp-tr
SSp-un
VISC
AUDd
AUDp
AUDpo
AUDv
VISam
VISl
VISp
VISpl
VISpm
VISli
VISpor
ACAd
ORBvl
RSPagl
RSPd
VISa
VISrl
TEa
PERI
ECT
ENTl
ENTm
PAR
POST
CLA
LA
CP
STR
GPe
GPi
SI
VPL
VPM
PoT
PP
MG
MGv
LGd
PO
POL
SGN
LD
PIL
RT
IGL
LGv
SubG
ZI
SCs
IC
NB
SAG
SNr
MRN
SCm
PAG
APN
NOT
PPT
CUN
NLL
SOC
PG
TRN
PRNr
DCO
VCO
NTB
IRN
MARN
MDRN
PARN
PGRNd
PGRNl
MV
F
BAR
Ipsilateral
Contralateral
ETd
ETi
ETd
ETi
Olfactory Areas
Hippocampus
Cerebral Nuclei
Thalamus
Hypothalamus
Midbrain
PONS
Medulla
FRP
MOp
MOs
SSp-n
SSp-bfd
SSp-ll
SSp-m
SSp-ul
SSp-tr
SSp-un
SSs
GU
VISC
AUDd
AUDp
AUDpo
AUDv
VISal
VISam
VISl
VISp
VISpm
VISli
VISpor
ACAd
PL
ORBl
ORBm
ORBvl
AId
AIv
RSPagl
RSPd
RSPv
VISa
VISrl
TEa
PERI
ECT
PIR
ENTl
CLA
CP
STR
ACB
CEA
GPe
VAL
VM
VPL
VPM
VPMpc
PoT
SPFp
MG
MGv
LGd
LP
PO
POL
SGN
LD
MD
SMT
PCN
CL
PF
PIL
RT
ZI
SCs
SNr
MRN
SCm
PAG
APN
NPC
RN
PPN
PSV
PB
PG
PRNc
TRN
CS
PRNr
NTB
SPVO
GRN
IRN
MARN
MDRN
PARN
pyd
G
VIS
ETi
74%
26%
ETd
Thalamus
FO
HO
Midbrain
PONS
73%
27%
82%
18%
82%
18%
99%
1%
H
AUD
ETi
61%
39%
ETd
Lemniscal centers
Thalamus
FO
HO
Midbrain
PONS
Medulla/ Spinal Cord
89%
11%
58%
42%
91%
9%
78%
22%
97%
3%
80%
20%
I
BAR
ETi
62%
38%
ETd
Lemniscal centers
Thalamus
FO
HO
Midbrain
PONS
Medulla/ Spinal Cord
69%
31%
55%
45%
78%
22%
64%
36%
91%
9%
86%
14%

Figure 4

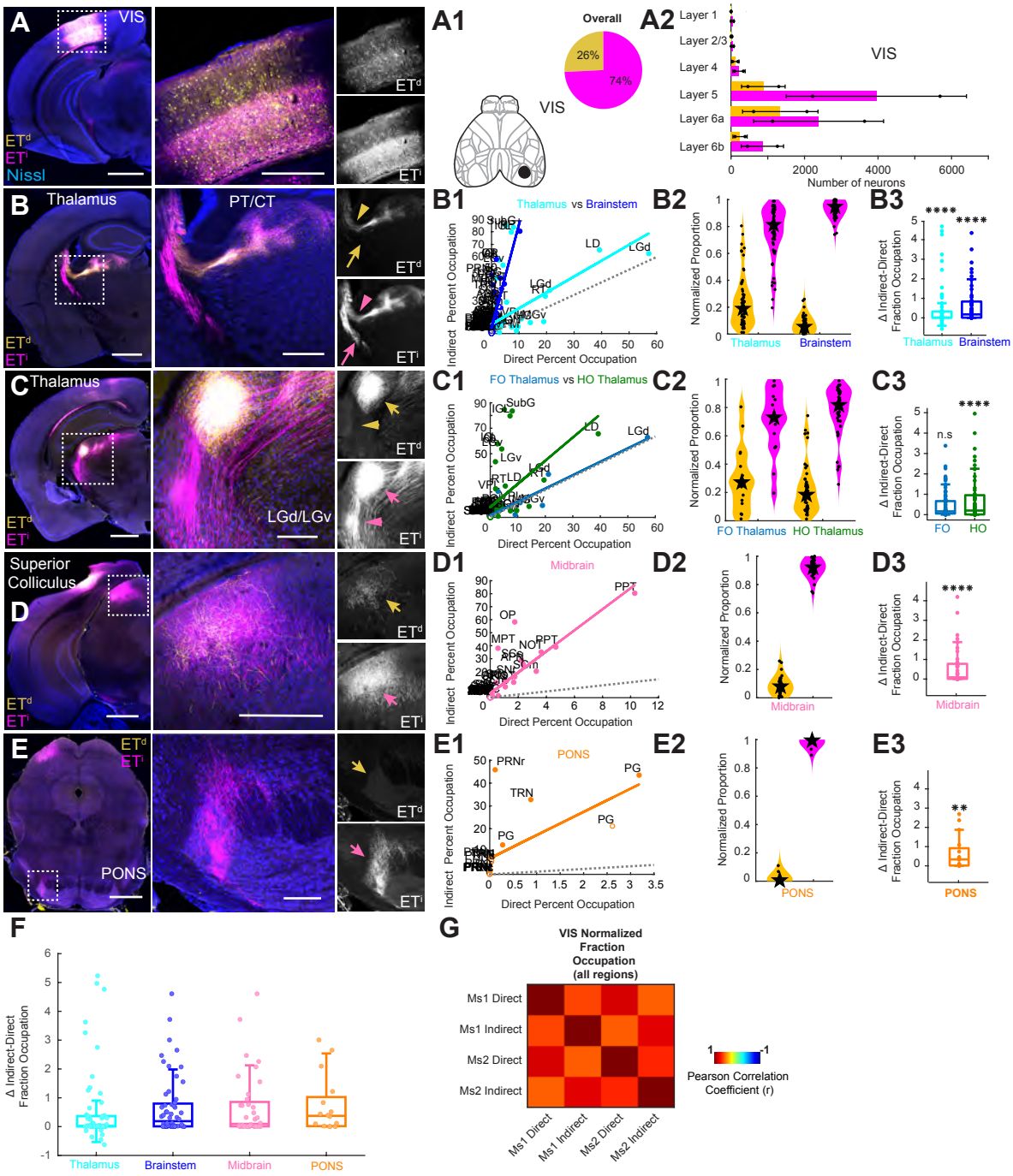

Figure S6, Related to Figure 4

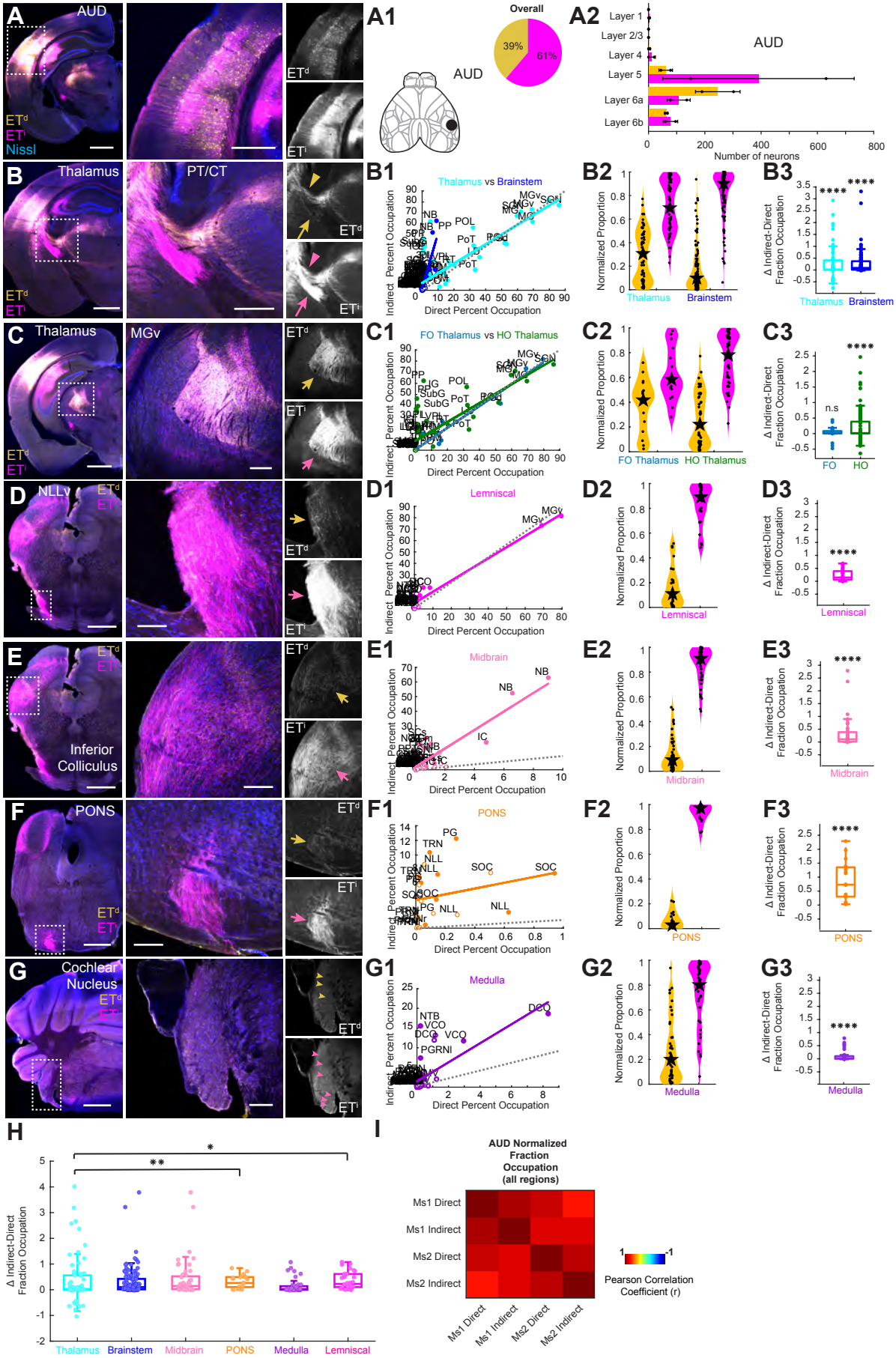

Figure S7, Related to Figure 4

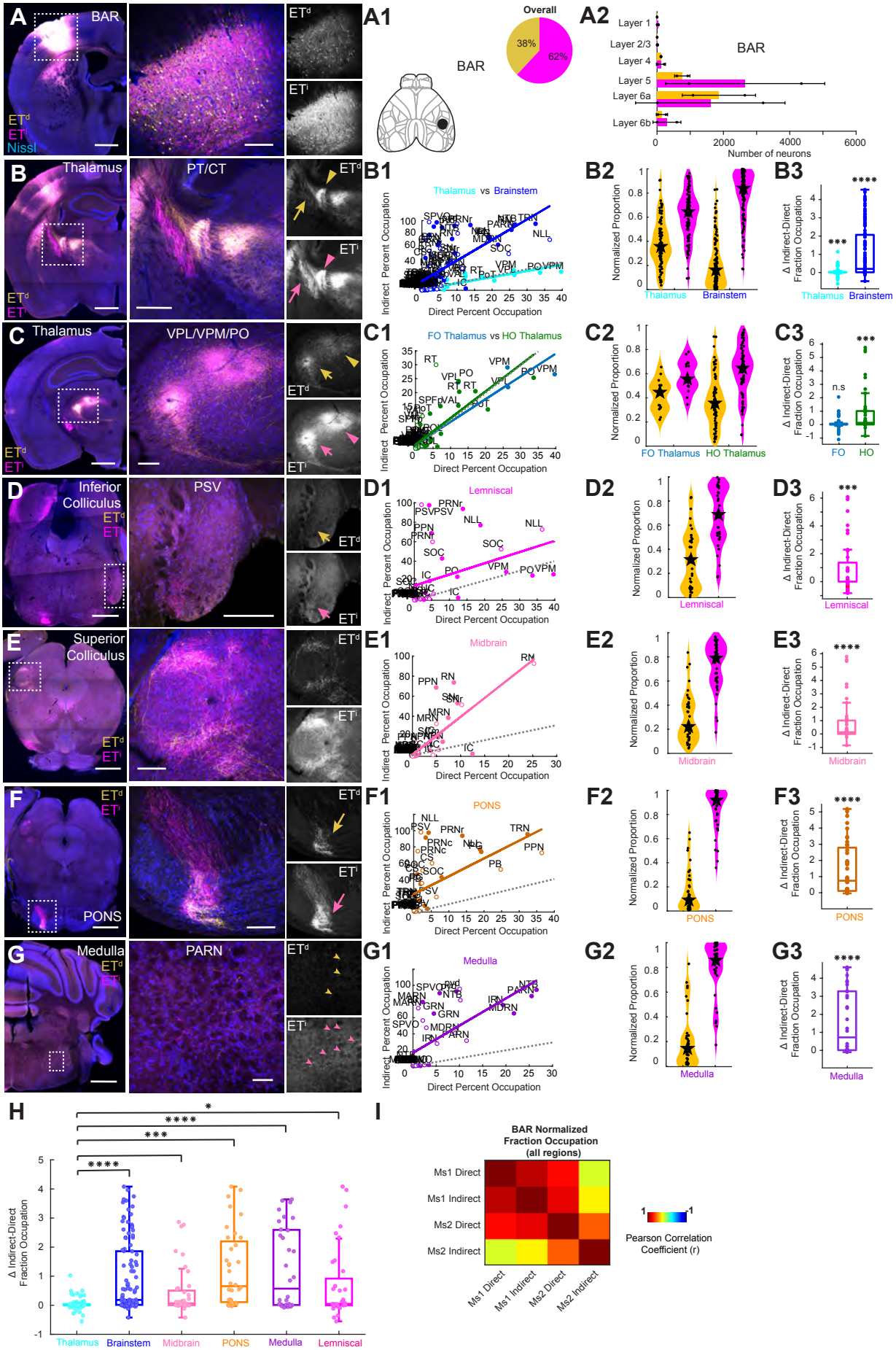

Figure S8, Related to Figure 4

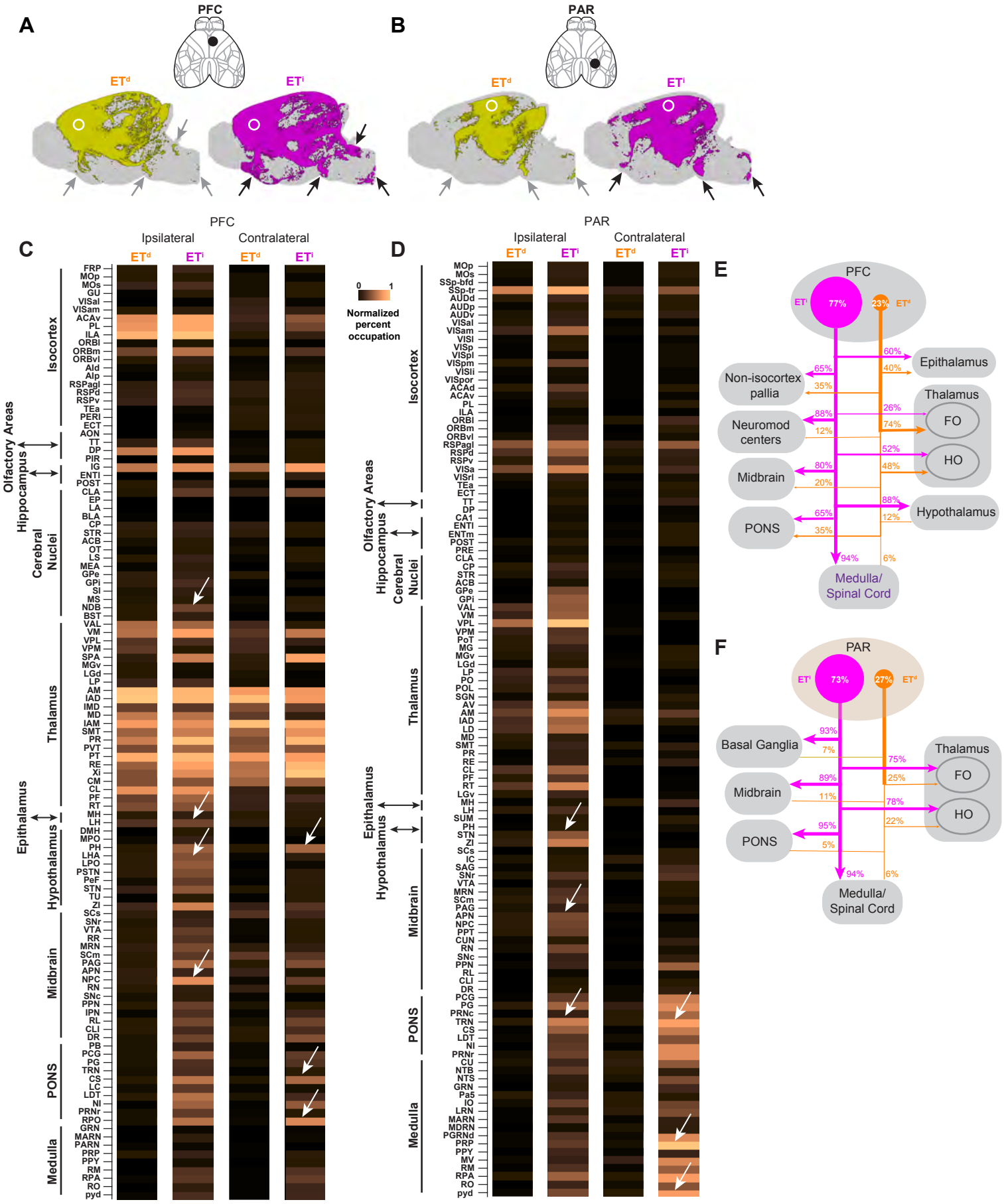
A
PFC
ETd
ETi
B
PAR
ETd
ETi
C
PFC
Ipsilateral
Contralateral
ETd
ETi
ETd
ETi
Olfactory Areas
Hippocampus
Cerebral Nuclei
Isocortex
Thalamus
Epithalamus
Hypothalamus
Midbrain
PONS
Medulla
0
1
Normalized percent occupation
D
PAR
Ipsilateral
Contralateral
ETd
ETi
ETd
ETi
E
PFC
ETi
77%
23%
ETd
60%
40%
Epithalamus
65%
35%
Non-isocortex pallia
Thalamus
88%
12%
Neuromod centers
26%
74%
FO
52%
48%
HO
80%
20%
Midbrain
88%
12%
Hypothalamus
65%
35%
PONS
94%
6%
Medulla/ Spinal Cord
F
PAR
ETi
73%
27%
ETd
93%
7%
Basal Ganglia
Thalamus
75%
25%
FO
89%
11%
Midbrain
78%
22%
HO
95%
5%
PONS
94%
6%
Medulla/ Spinal Cord

Figure 5

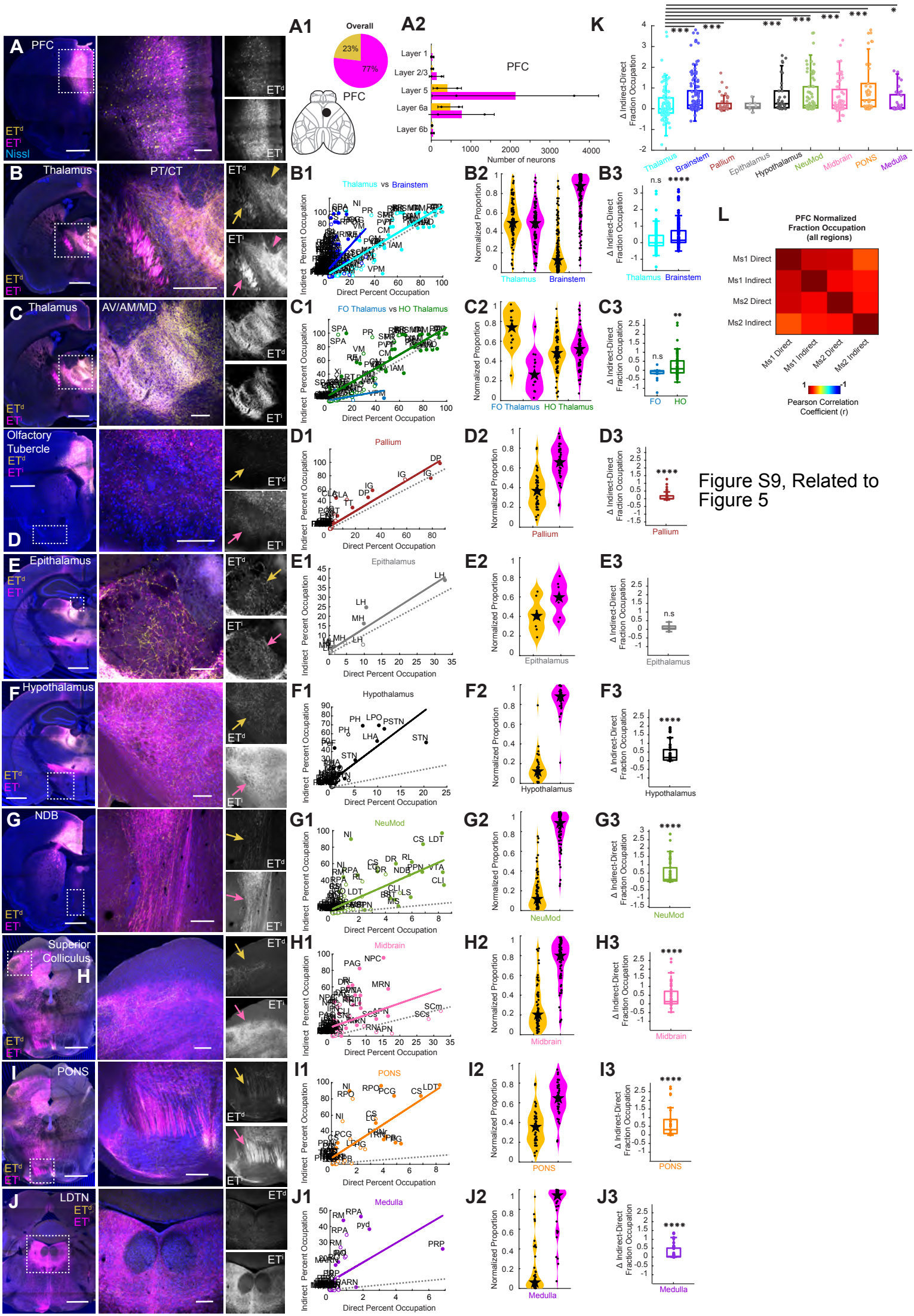

Figure S9, Related to Figure 5

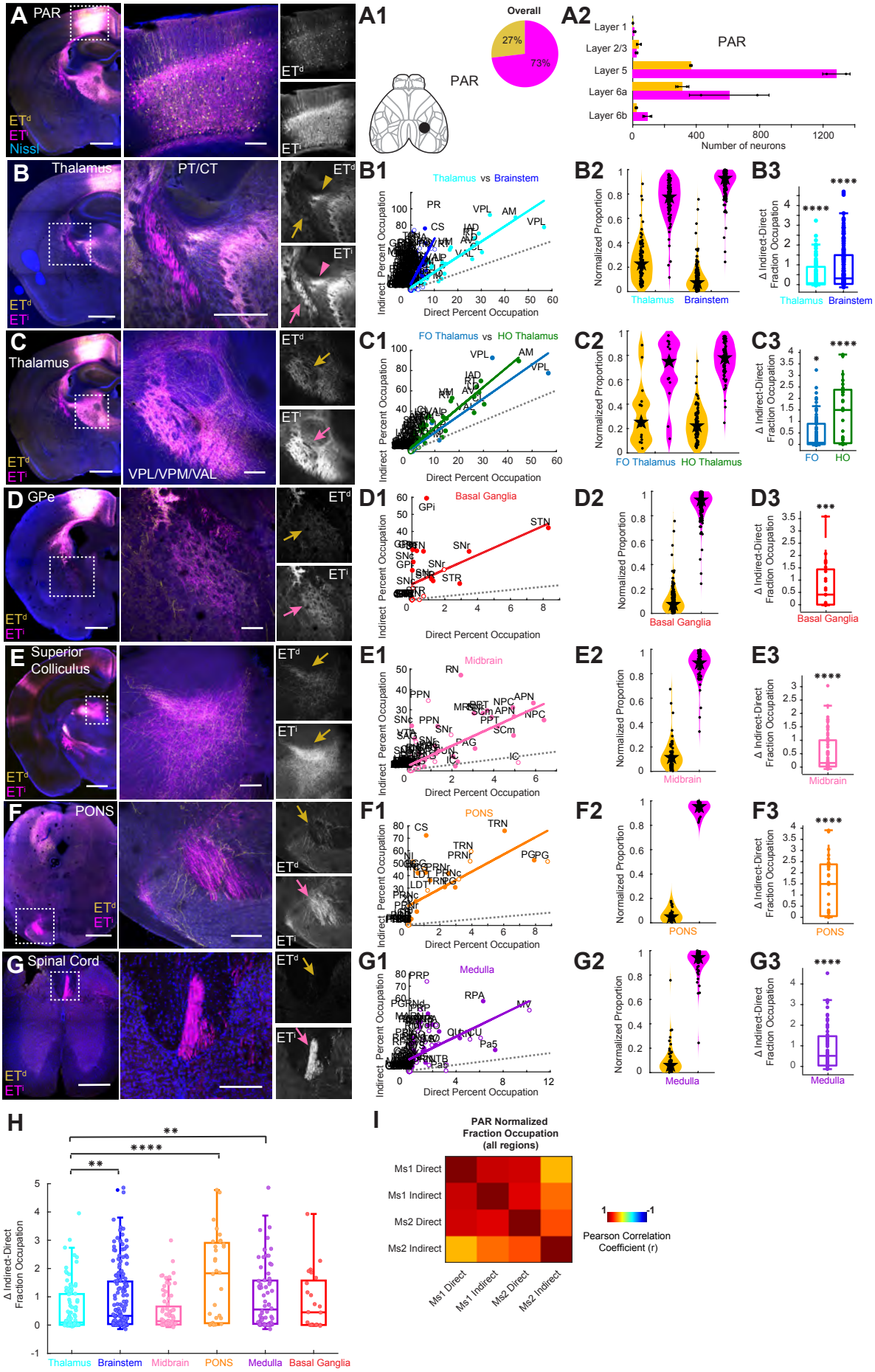

Figure S10, Related to Figure 5

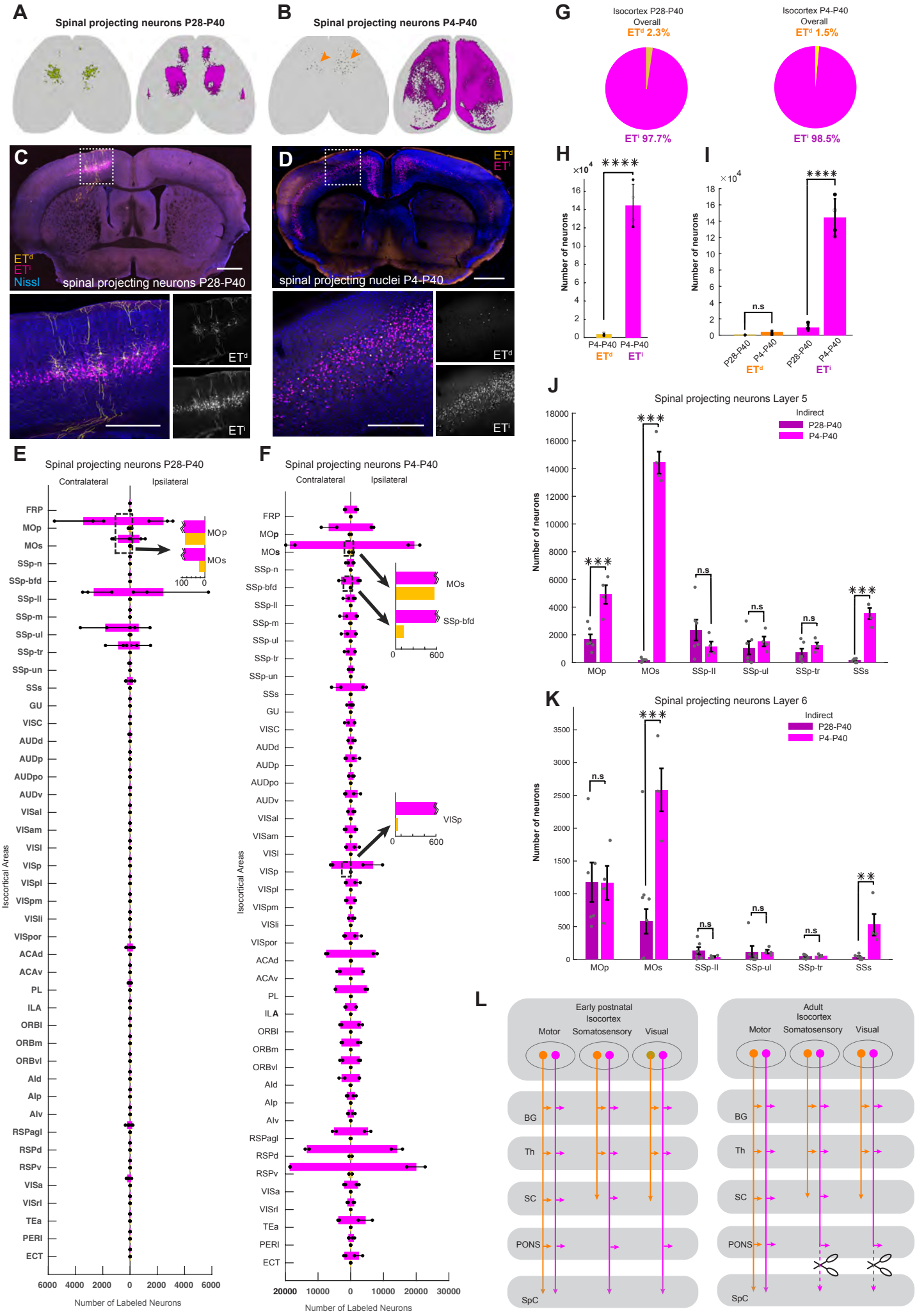
A
Spinal projecting neurons P28-P40
B
Spinal projecting neurons P4-P40
C
ETd
ETi
Nissl
spinal projecting neurons P28-P40
D
ETd
ETi
spinal projecting nuclei P4-P40
ETd
ETi
E
Spinal projecting neurons P28-P40
Contralateral
Ipsilateral
Isocortical Areas
Number of Labeled Neurons
F
Spinal projecting neurons P4-P40
Contralateral
Ipsilateral
Isocortical Areas
Number of Labeled Neurons
G
Isocortex P28-P40
Overall
ETd 2.3%
ETi 97.7%
Isocortex P4-P40
Overall
ETd 1.5%
ETi 98.5%
H
Number of neurons
P4-P40 P4-P40
ETd ETi
I
Number of neurons
n.s
P28-P40 P4-P40 P28-P40 P4-P40
ETd ETi
J
Spinal projecting neurons Layer 5
Indirect
P28-P40
P4-P40
Number of neurons
MOp MOs SSp-ll SSp-ul SSp-tr SSs
K
Spinal projecting neurons Layer 6
Indirect
P28-P40
P4-P40
Number of neurons
MOp MOs SSp-ll SSp-ul SSp-tr SSs
L
Early postnatal
Isocortex
Motor Somatosensory Visual
BG
Th
SC
PONS
SpC
Adult
Isocortex
Motor Somatosensory Visual
BG
Th
SC
PONS
SpC

Figure 6

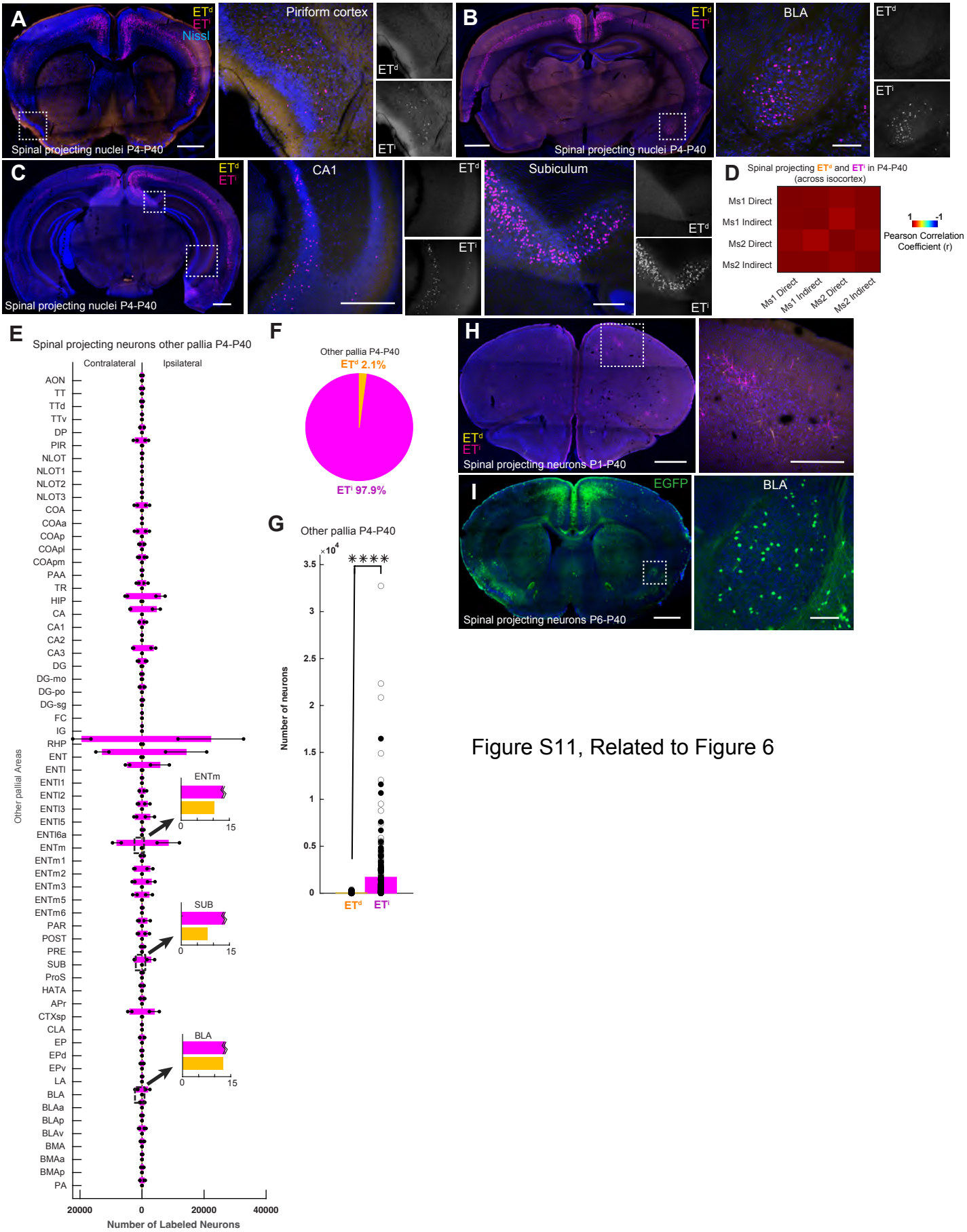

Figure S11, Related to Figure 6

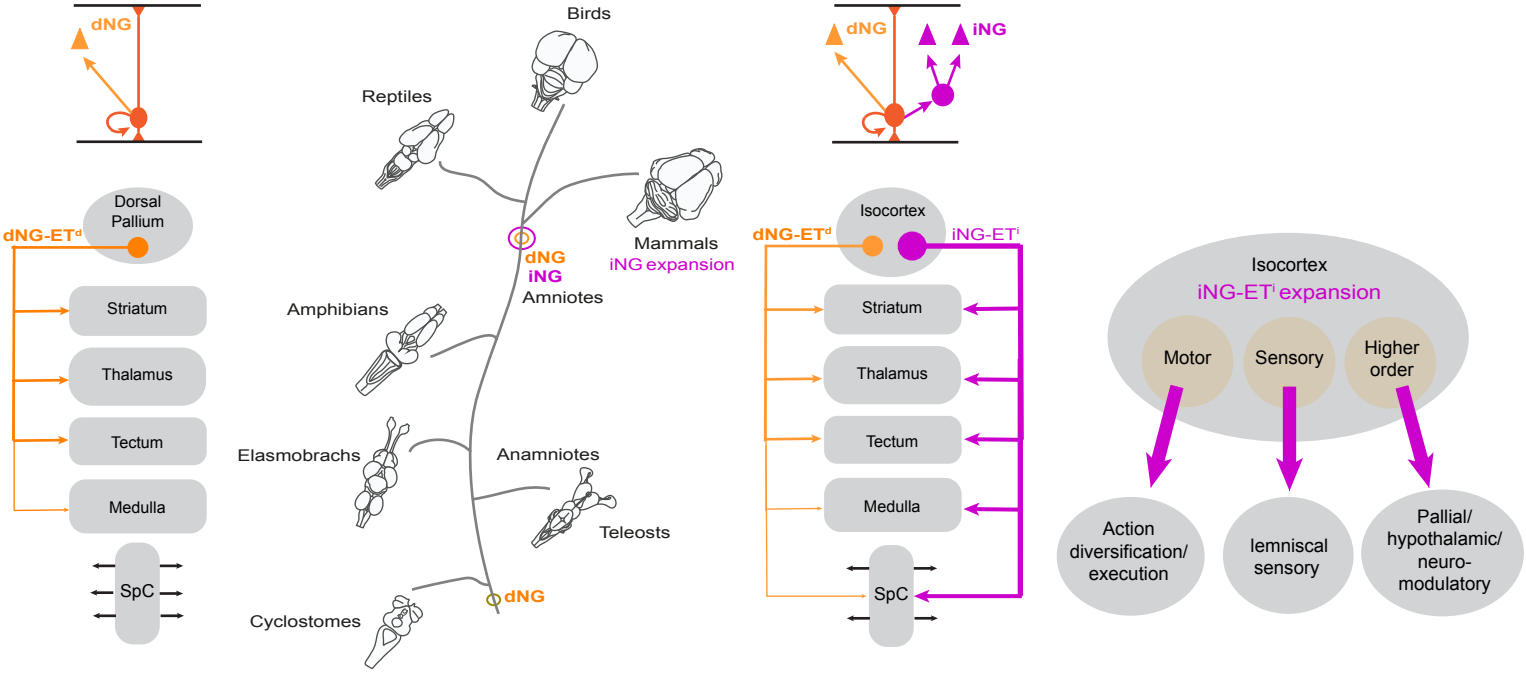
dNG
Dorsal Pallium
dNG-ET^d
Striatum
Thalamus
Tectum
Medulla
SpC
Birds
Reptiles
Mammals
iNG expansion
dNG
iNG
Amniotes
Amphibians
Elasmobrachs
Anamniotes
Teleosts
Cyclostomes
dNG
dNG
iNG
Isocortex
dNG-ET^d
iNG-ET^i
Striatum
Thalamus
Tectum
Medulla
SpC
Isocortex
iNG-ET^i expansion
Motor
Sensory
Higher order
Action diversification/ execution
lemniscal sensory
Pallial/ hypothalamic/ neuro-modulatory

Figure 7

Figure Legends

Figure 1. Genetic strategy for differential targeting of *Fezf2*$^+$ ET^d and ET^i PNs in the same mouse.

(A) Schematic of *Fezf2-tTA-CreER (FezF2TC)* knockin allele where a *frt-tTA-frt-CreER* cassette was inserted in frame before the STOP codon of *Fezf2* gene. In *FezfTC;Tbr2-Flp* double-allele mice, dNG-derived ET^d express *tTA* while iNG-derived ET^i express *CreER*, as *tTA* is removed by *Tbr2-Flp* in IPs. Postnatal injection of *AAV-TRE-GFP* and *AAV-FLEX-RFP* in cortex differentially label ET^d and ET^i, respectively.

(B) Cortex wide labelling of ET^d and ET^i neurons through retro-orbital co-injections of *AAVPHP.eB-TRE-EGFP* and *AAVPHP.eB-FLEX-tdTomato* in *FezfTC;Tbr2-Flp* mice.

(C) Schematic of stereotactic AAV injection to label ET^d and ET^i using *FezF2-TC;Tbr2Flp* mice in the RFO, BAR, and VIS. Labeled ET neurons across the three areas consist of 24% ET^d and 76% ET^i.

(C1-C3) Focal labelling of ET^d (yellow) and ET^i (magenta) in RFO (C1) BAR (C2), and VIS (C3). Significantly more number of ET^i than ET^d neurons were labelled in all three areas (bottom panels).

Abbreviations: RFO – rostral forelimb orofacial area in motor cortex; BAR – barrel cortex; VIS – visual cortex; dNG – direct neurogenesis; iNG - indirect neurogenesis; ET^d – direct neurogenesis generated extratelencephalic neuron; ET^i – indirect neurogenesis generated extratelencephalic neuron; RG - radial glia; IP – intermediate progenitor. Scatter points in bar plots indicate individual data points. Error bars indicate SD. Statistical tests used two-sample t-tests (p-values: *$p < 0.05$, n.s = not significant) Scalebars in (B) 1 mm (C1-C3) 500 µm.

Figure 2. Amplification, diversification and innovation of ET^i over ET^d subclasses

(A-D) Retrograde labelling of ET^d and ET^i from superior colliculus (A), pontine nuclei (B), medulla (C), and cervical spinal cord (D). Injection schematics are in top left. Pie charts show the overall proportion of labeled ET^d and ET^i across isocortex for each injection site. Bottom row shows the 3D rendering of the distribution of labelled ET^d and ET^i neurons across isocortex. Green arrows indicate example areas with both ET^d and ET^i; red arrows indicate example areas with significantly more or entirely ET^i.

(E-H) Retrogradely labelled ET^d and ET^i for (E) colliculus-projecting, (F) pons-projecting, (G) medullary-projecting and (H) spinal-projecting neurons across the isocortex.

(I-L) Left panel*s*: Bar plots showing that the number of retrogradely labeled ET^i is significantly larger than that of ET^d across isocortex from each of the four injection sites. Right panels: Paired bar plots comparing the expected proportions of ET^d and ET^i (based on their approximate overall 1:3 cell number ratio) to the actual labelled proportions for each injection site. There is a significant increase in the proportion of actual ET^i over expected ET^i for all 4 injection sites. On the other hand, there is a significant decrease of proportion of actual ET^d over expected ET^d.

(M-O) Bar plots of retrogradely labelled ET neuron numbers for areas with exclusively ET^i and no ET^d from pontine (M), medullary (N), and spinal (O) injections, suggesting the innovation of novel ET^i over ET^d projection types in these areas. Note the abundance of sensory (green font) and higher order (orange font) areas. There were no areas with exclusively ET^i labeling from collicular injection.

(P) Schematic representing amplification, diversification and innovation of ET subclasses by iNG. Amplification is simple generation of copies of ET^d by ET^i; Diversification is generation of distinct

projection subclasses by ET^i while innovation reflects generation of novel projection classes which are exclusively ET^i.

Abbreviations: BG – basal ganglia; Th – thalamus; SC – superior colliculus; PONS – pontine nuclei; SpC – spinal cord. For abbreviations in (M-O) see Table S1. Scatter points in bar plots indicate individual data. Filled markers indicate ipsilateral and open markers indicate contralateral data.Error bars indicate SD. Statistical tests used: two-sample t-tests (p-values: *$p < 0.05$, ****$p < 0.0001$, n.s = not significant) Scalebars in (E-H, top panels) 1 mm (E-H, bottom panels) 500 µm.

Figure 3. Amplification and diversification of ET^i over ET^d projections from motor areas.

(A-C). Schematic of anterograde AAV injection site and 3D rendering in the sagittal plane for ET^d and ET^i axonal projections from (RFO, A), (CFA, B) and (MOs, C). White circles indicate injection sites. Black arrows indicate examples of greatly expanded ET^i projections to more distal targets.

(D-F). Heatmaps showing normalized percent occupation of target structures across the brain from ET^d and ET^i for ipsilateral and contralateral sides of the injection sites for RFO (D) CFA (E) MOs (F). White arrows indicate example areas with significant increase in percent occupation by ET^i over ET^d. Note the substantial increase of ET^i projections to several brainstem areas and the pyramidal tract.

(G-I). Schematics showing the amplification and diversification of ET^i over ET^d neurons and projections from the three motor areas scaled to the proportion of ET^d and ET^i labelled at the injection sites. Note the significantly expanded ET^i projections to the BG (action selection), and medulla and SpC (action diversification and execution) areas while having similar projections as ET^d to thalamus.

Abbreviations: RFO – rostral forelimb orofacial area in the motor cortex; CFA – caudal forelimb area; MOs – secondary motor area; BG – basal ganglia; SpC – spinal cord. For abbreviations in (D-F) see Table S1.

Figure 4. Amplification, diversification and innovation of ET^i over ET^d projections from Sensory areas.

(A-C). Schematic of anterograde AAV injection site and 3D rendering in the sagittal plane for ET^d and ET^i axonal projections from (VIS, A), (AUD, B) and (BAR, C). White circles indicate injection sites. Black arrows indicate examples of greatly expanded ET^i projections to more distal targets.

(D-F). Heatmaps showing normalized percent occupation of target structures across the brain from ET^d and ET^i for both ipsilateral and contralateral sides of the injection sites for VIS (D) AUD (E), and BAR (D). White arrows indicate example areas with significant increase in percent occupation by ET^i over ET^d. Note the increased or exclusive projections to PONS from ET^i in all three areas while similar increased projections to medulla from ET^i from BAR.

(G-I). Schematics showing the amplification and diversification of ET^i over ET^d neurons and projections from the three sensory areas scaled to the proportion of ET^d and ET^i labelled at the injection sites. Note that the corticopontine projections are almost exclusively ET^i projections and the massive ET^i elaboration to lemniscal centers. There is also an expansion of ET^i projections to medulla and SpC, similar to motor areas from BAR.

Abbreviations: VIS – visual cortex; AUD – auditory cortex; BAR – barrel cortex; PONS – pontine nuclei; SpC – spinal cord. For abbreviations in (D-F) see Table S1.

Figure 5. Amplification, diversification and innovation of ET^i over ET^d projections from higher order areas.

(A-B). Schematic of AAV injection site and 3D renderings in the sagittal plane for ET^d and ET^i axonal projections from (PFC, A) and (PAR, B). White circles indicate injection sites. Black arrows indicate examples of greatly expanded ET^i projections to more distal targets.

(C-D). Heatmaps showing normalized percent occupation of target structures across the brain from ET^d and ET^i for both ipsilateral and contralateral sides of the injection sites for PFC (C) and PAR (D). White arrows indicate example areas with significant increase in percent occupation by ET^i over ET^d. Note the significantly increased ET^i projections to hypothalamus, other pallial areas and the brainstem, while similar projections as ET^d in the thalamus from PFC. For PAR note the increased ET^i projections to BG and brainstem areas.

(E-F). Schematics showing the amplification and diversification of ET^i over ET^d neurons and projections from PFC and PAR scaled to the proportion of ET^d and ET^i labelled at the injection sites. Note the expansion of ET^i projections to neuromodulatory, hypothalamic and other pallial areas while having similar proportions as ET^d to the epithalamus from PFC. Note motor-like expansion of ET^i projections to BG and medulla/SpC from PAR.

Abbreviations: PFC – prefrontal cortex; PAR – parietal cortex; BG – basal ganglia; SpC – spinal cord. For abbreviations in (C-D) see Table S1.

Figure 6. Selective axon pruning in ET^i but not ET^d neuron during early postnatal development shapes the areal distribution of ET^i

(A-B) 3D renderings of retrogradely labelled ET^d (yellow) and ET^i (magenta) spinal projecting neurons/nuclei across isocortex from retrograde AAV injections into the cervical spinal cord of P28-P40 (A) and P4-P40 (B) mice.

(C-D) Retrogradely labelled ET^d and ET^i spinal projecting neurons (C) or nuclei (D) from cSpC injections in P28-P40 (C) and P4-P40 (D) mice. Scale bars: 1 mm in top and 500um in bottom panels.

(E-F) Bar plots showing number of retrogradely labelled ET^d (yellow) and ET^i (magenta) spinal projecting neurons across different isocortical areas. Error bars represent standard deviations. Zoomed in views magnify selected areas (in dotted black rectangle) showing low ET^d numbers compared to ET^i. The zoomed ET^i bar plots are truncated to show ET^d cell numbers.

(G) Pie charts showing the proportion of ET^d and ET^i spinal projecting neurons across isocortex from injections into the cervical spinal cord of P28-P40 (left) P4-P40 (right) mice.

(H) Bar plots showing that the number of retrogradely labelled ET^i spinal projecting neurons is significantly larger than the number of ET^d spinal projecting neurons across isocortex from injections into cSpC of P4-P40 mice.

(I) Bar plots showing that number of ET^i spinal projecting neurons across isocortex from cSpC injections in P4-P40 mice is significantly more than that of cSpC injections in P28-P40 mice, while there is no significant change for ET^d spinal projecting neurons between the two.

(J) Paired bar plots comparing number of retrogradely labelled layer 5 spinal projecting neurons/nuclei in MOp, MOs, SSp-ll, SSp-ul, SSp-tr and SSs between P28-P40 and P4-P40 mice. The P4-P40 mice

had significantly more nuclei in MOp, MOs and SSs while there were no significant changes in other areas.

(K) Paired bar plots comparing number of retrogradely labelled layer 6 spinal projecting neurons/nuclei in MOp, MOs, SSp-ll, SSp-ul, SSp-tr and SSs between P28-P40 and P4-P40 mice. The P4-P40 mice had significantly more nuclei in MOs and SSs while there were no significant changes in other areas.

(O) A schematic showing selective axon pruning in corticospinal ET^i but not ET^d neurons during early postnatal development more evident in mid and posterior areas of the isocortex , which shapes the projection patterns and areal distribution of ET^i in mature cortex.

Abbreviations: P28-P40 – mice with injections on P28 and harvested at P40; P4-P40 – mice with injections at P4 and harvested at P40; cSpC – cervical spinal cord. For abbreviations in (E-F, J-K) see Table S1. Error bars indicate SD. Scatter points indicate individual data.Filled markers indicate ipsilateral and open markers indicate contralateral data Statistical tests used: (H, J, K) two-sample t-test; (I) two-sample t-test and Mann-Whitney U test (p-values: *$p < 0.05$, **$p < 0.01$, ***$p < 0.001$,****$p < 0.0001$, n.s = not significant)

Figure 7. Schematic summary of the evolutionary origin and development impact of dNG and iNG that shape the amplification, diversification and innovation of corticofugal projection neurons.

While dNG evolved before the dawn of vertebrates, iNG emerged from amniotes and greatly expanded in mammals. In early vertebrates (left), the pallium does have a basic dNG- ET^d efferent projection pattern from the pallium to downstream motor centers, in mammals (right), dNG-ET^d and the hugely expanded iNG-ET^i are intermixed and form mosaic circuits. While dNG-ET^d largely targets conserved structures in the forebrain and midbrain, iNG-ET^i massively amplifies, diversifies and *innovates* projection classes to brainstem and spinal cord. Moreover, iNG-ET^i expands projections in an area specific manner (extreme right) reflected in the expanded projections to action selection, diversification and execution centers from the motor areas; to sensory processing centers along the lemniscal pathways from the sensory areas; and to neuromodulatory, hypothalamic and other pallial centers from higher order areas of the isocortex.

Abbreviations: dNG – direct neurogenesis; iNG - indirect neurogenesis; ET^d – direct neurogenesis generated extratelencephalic neuron; ET^i – indirect neurogenesis generated extratelencephalic neuron; SpC – spinal cord.

Supplemental Figure Legends

Figure S1. Validation of the *FezFTC;Tbr2Flp* mice for viral access to capture ET^d and ET^i, Related to Figure 1.

(A) Schematic of strategy for validating the *FezF2-TC* line. Without the*Tbr2-Flp* allele *FezF2-TC* drives *tTA* expression in all *FezF2*+ neurons, which can be labelled by injection of *AAV-TRE-EGFP*.

(B-C) The vast majority of the EGFP-labelled neurons in the deep layers overlap with *in situ* detection of *FezF2* mRNA (red) verifying that they are *FezF2*+ (yellow).

(D-G) Strategy and result of checking for non-specific labelling for *AAV-TRE-EGFP*. Injection of *AAV9-TRE-EGFP* in *LSL-Flp* mice, which do not express tTA (D), did not result in prominent GFP expression. Faint GFP signals at the injection site (E) resulted from low level leakage of *TRE-EGFP* but did not label any corticofugal axons in pons (F) and medulla (G) even after antibody amplification of EGFP signal.

(H-I) Strategy and result for checking non-specific labelling for *AAV-CAG-FLEX-tdTomato*. We inject *AAV9-CAG-FLEX-tdTomato* together with *AAV9-TRE-EGFP* in *FezF2-TC* mice as in (A). All *FezF2*+ neurons are labelled with EGFP at the injection site. There is negligible labelling of *tdTomato, as* there is no *Cre* expression in the *FezF2-TC*, indicating that there is almost no leaky expression.

(J) (left) Schematic of a previous strategy wherein dNG and iNG can be simultaneously visualized by a genetic fate-mapping scheme using the IS2 reporter with *FezF2-CreER* (RG) and *Tbr2-Flp* (IP) drivers: dNG-ET^d (*Fezf2*$^+$/*Tbr2*$^-$) is labeled by RFP through "Cre-NOT-Flp" subtraction; iNG-ET^i (*FezF2*$^+$/*Tbr2*$^+$) is labeled by EGFP through "Cre-AND-Flp" intersection (see Huilgol 2023). (right) Overall proportions of ET^d and ET^i neurons from RFO, BAR and VIS areas was 1:3.

(K-M) (left) We compared sections from RFO (K), BAR (L) and VIS (M) corresponding to the sections in Figure 1C-C3. (right) The number of ET^i neurons were significantly more than ET^d for RFO and BAR.

(N-N2) Comparing proportions of dNG-ET^d and iNG-ET^i labelled from the new and old strategies: viral targeting in *FezFTC;Tbr2Flp* in Figure 1A and *FezFTC;Tbr2Flp;IS2* in (J), showed no significant differences showing both strategies are comparable and consistent for (N) RFO, (N1) BAR and (N2) VIS.

Abbreviations: RFO – rostral forelimb orofacial area; BAR – barrel cortex; VIS – visual cortex; Error bars indicate SD. Scatter points indicate individual data. Statistical tests used: two-sample t-tests (p-values: *$p < 0.05$, **$p < 0.01$, n.s = not significant).Scalebars in (B,E,I) 500 µm (F,G) 1 mm.

Figure S2. ET^d and ET^i collicular-, pontine-, medulla- and spinal- projecting neurons. Related to Figure 2.

(A-D) Bar plots of retrogradely labelled ET^d (yellow) and ET^i (magenta) neuron numbers across different areas of the isocortex from collicular (A), pontine (B), medulla (C), and cervical spinal cord (D) injections. X-axis is shown in a Log_{10} scale.

(E) Correlation matrix heatmap showing pairwise Pearson correlations between number of retrogradely labelled ET^d and ET^i neurons across all areas of the isocortex from 2-3 mice each from collicular, pontine, medulla, and cervical spinal cord injections.

Abbreviations for all isocortical regions in (A-D) are listed in Table S1. Error-bars represent SEM.

Figure S3. Predominant ET^i over ET^d subcortical projections from RFO, Related to Figure 3

(A) AAV injection in the RFO labeled ET^d (yellow) and ET^i (magenta).

(A1) Left, location of the injection site shown on a schematic of the dorsal cortex. Right, pie chart of proportion of ET^d and ET^i neurons labelled at the injection site.

(A2) Bar plots of layer-wise counts of labelled ET^d and ET^i neurons in the injection site (n = 2 mice).

(B) PT and CT fiber bundles with ET^d and ET^i projections from RFO. Notice both ET^d and ET^i projections in CT (arrowhead) while largely ET^i in PT (arrow).

(C) Dense ET^d and ET^i projections to the thalamus, including VPM/VPL.

(D) Dense ET^i but weak ET^d projections to the GPe.

(E) Stronger ET^i over ET^d projections to the superior colliculus.

(F) Strong ET^i but weak ET^d projections to the PONS.

(G) Strong ET^i but nearly no ET^d projections to the spinal cord.

(B1-G1) Scatter plots with linear regression of normalized fraction occupations of RFO ET^d and ET^i projections to target regions (B1) thalamus and brainstem, (C1) first order (FO) and higher order (HO) thalamus, (D1) basal ganglia, (E1) midbrain, (F1) PONS, (G1) medulla.

(B2-G2) Violin plots showing normalized percent occupation for RFO ET^d and ET^i projections with the star indicating the median and black circles showing individual values for subregions within target regions of (B2) thalamus and brainstem (C2) first order (FO) and higher order (HO) thalamus (D2) basal ganglia (E2) midbrain (F2) PONS (G2) medulla.

(B3-G3) Box plots of Z-score normalized percent occupation differences between ET^i and ET^d projections from RFO to (B3) thalamus and brainstem, (C3) first order (FO) and higher order (HO) thalamus, (D3) basal ganglia, (E3) midbrain, (F3) PONS, (G3) medulla. p-values reflect significant within region differences.

(H) Box plots of Z-score normalized percent occupation differences between ET^i and ET^d projections from RFO for brainstem, midbrain, PONS, medulla and BG with post-hoc comparisons to thalamus, following a multiple comparisons test ($p < 0.05$) to assess statistical differences among different projection target regions. The brainstem, medulla and BG regions showed significantly more iNG-ET^i projections than thalamus.

(I) Correlation matrix heatmap showing pairwise Pearson correlations between ET^d and ET^i normalized fraction occupation across all areas for projections from RFO across two mice used for LightSheet Imaging.

Abbreviations: RFO – rostral forelimb orofacial area; FO – first order thalamic nuclei; HO- higher order thalamic nuclei; VPM – ventral posterior medial nucleus; VPL – ventral posterior lateral nucleus; PO – posterior thalamic nucleus GPe- Globus pallidus externa; PONS – pontine nuclei; BG – basal ganglia. Subregions for each target region are listed in Table S1. Scatter points in scatter plots, violin plots and box plots represent individual subregion percent occupation (normalized or raw) values, with filled markers for ipsilateral and open markers for contralateral data. Regression lines indicate overall correlation trends. Dotted grey line indicates the line of equality. Interquartile range in box plots is 25th–75th percentiles. Statistical tests used one-sample t-test, Wilcoxon signed-rank test, Kruskal–Wallis test, Wilcoxon rank-sum test and Kolmogorov-Smirnov test (p-values: *$p < 0.05$, **$p < 0.01$, ***$p < 0.001$, ****$p < 0.0001$, n.s = not significant) Scalebars in (A-F) 1 mm; (G, A right, B right) 500 µm; (C right, E right, F right) 200 µm; (D right, G right) 100 µm.

Figure S4. Predominant ET^i over ET^d subcortical projections from CFA, Related to Figure 3

(A) AAV injection in the CFA labeled ET^d (yellow) and ET^i (magenta).

(A1) (left) Location of the injection site shown on a schematic of dorsal cortex. (right) Pie chart of proportion of ET^d and ET^i neurons labelled at the injection site.

(A2) Bar plots of layer-wise counts of labelled ET^d and ET^i neurons in the injection site (n = 2 mice).

(B) PT and CT fiber bundles with ET^d and ET^i projections from CFA. Notice both ET^d and ET^i projections in CT (arrowhead) while largely ET^i in PT (arrow).

(C) Dense ET^d and ET^i projections to the thalamus, including VPM.

(D) Dense ET^i but weak ET^d projections to the SNr.

(E) Stronger ET^i over ET^d projections to the superior colliculus.

(F) Strong ET^i but weak ET^d projections to the PONS.

(G) Strong ET^i but nearly no ET^d projections to the spinal cord.

(B1-G1) Scatter plots with linear regression of normalized fraction occupations of CFA ET^d and ET^i projections to target regions (B1) thalamus and brainstem, (C1) first order (FO) and higher order (HO) thalamus, (D1) basal ganglia, (E1) midbrain, (F1) PONS, (G1) medulla.

(B2-G2) Violin plots showing normalized percent occupation for CFA ET^d and ET^i projections with the Star indicating the median and black circles showing individual values for subregions within target regions of (B2) thalamus and brainstem (C2) first order (FO) and higher order (HO) thalamus (D2) basal ganglia (E2) midbrain (F2) PONS (G2) medulla.

(B3-G3) Box plots of Z-score normalized percent occupation differences between ET^i and ET^d projections from CFA to (B3) thalamus and brainstem, (C3) first order (FO) and higher order (HO) thalamus, (D3) basal ganglia, (E3) midbrain, (F3) PONS, (G3) medulla. p-values reflect significant within region differences.

(H) Box plots of Z-score normalized percent occupation differences between ET^i and ET^d projections from CFA for brainstem, midbrain, PONS, medulla and BG with post-hoc comparisons to thalamus, following a multiple comparisons test ($p < 0.0001$) to assess statistical differences among different projection target regions. The brainstem, PONS, medulla and BG regions showed significantly more iNG-ET^i projections than thalamus.

(I) Correlation matrix heatmap showing pairwise Pearson correlations between ET^d and ET^i normalized fraction occupation across all areas for projections from CFA across two mice used for LightSheet Imaging.

Abbreviations: CFA – caudal forelimb area; FO – first order thalamic nuclei; HO- higher order thalamic nuclei; VPM – ventral posterior medial nucleus; PO – posterior thalamic nucleus SNr – substantia nigra *pars reticulata*; PONS – pontine nuclei; BG – basal ganglia. Subregions for each target region are listed in Table S1. Scatter points in scatter plots, violin plots and box plots represent individual subregion percent occupation (normalized or raw) values, with filled markers for ipsilateral and open markers for contralateral data. Regression lines indicate overall correlation trends. Dotted grey line indicates the line of equality. Interquartile range in box plots is 25th–75th percentiles. Statistical tests used one-sample t-test, Wilcoxon signed-rank test, Kruskal–Wallis test, Wilcoxon rank-sum test and Kolmogorov-Smirnov test (p-values: *$p < 0.05$, **$p < 0.01$, ***$p < 0.001$, ****$p < 0.0001$, n.s = not significant) Scalebars in (A-F) 1 mm; (G, A-B right) 500 µm; (C right, E right, G right) 250 µm; (D right, F right) 200 µm.

Figure S5. Predominant ET^i over ET^d subcortical projections from MOs, Related to Figure 3

(A) AAV injection in the MOs labeled ET^d (yellow) and ET^i (magenta).

(A1) Left, location of the injection site shown on a schematic of dorsal cortex. Right, pie chart of proportion of ET^d and ET^i neurons labelled at the injection site.

(A2) Bar plots of layer-wise counts of labelled ET^d and ET^i neurons in the injection site (n = 2 mice).

(B) PT and CT fiber bundles with ET^d and ET^i projections from MOs. Notice both ET^d and ET^i projections in CT (arrowhead) while largely ET^i in PT (arrow).

(C) Dense ET^d and ET^i projections to the thalamus, including PO/PCN.

(D) Dense ET^i but weak ET^d projections to the GPi.

(E) Stronger ET^i over ET^d projections to the superior colliculus.

(F) Strong ET^i but weak ET^d projections to the PONS.

(G) Strong ET^i but nearly no ET^d projections to the spinal cord.

(B1-G1) Scatter plots with linear regression of normalized fraction occupations of MOs ET^d and ET^i projections to target regions (B1) thalamus and brainstem, (C1) first order (FO) and higher order (HO) thalamus, (D1) basal ganglia, (E1) midbrain, (F1) PONS, (G1) medulla.

(B2-G2) Violin plots showing normalized percent occupation for MOs ET^d and ET^i projections with the Star indicating the median and black circles showing individual values for subregions within target regions of (B2) thalamus and brainstem (C2) first order (FO) and higher order (HO) thalamus (D2) basal ganglia (E2) midbrain (F2) PONS (G2) medulla.

(B3-G3) Box plots of Z-score normalized percent occupation differences between ET^i and ET^d projections from MOs to (B3) thalamus and brainstem, (C3) first order (FO) and higher order (HO) thalamus, (D3) basal ganglia, (E3) midbrain, (F3) PONS, (G3) medulla. p-values reflect significant within region differences.

(H) Box plots of Z-score normalized percent occupation differences between ET^i and ET^d projections from MOs for brainstem, midbrain, PONS, medulla and BG with post-hoc comparisons to thalamus, following a multiple comparisons test ($p = 0.0054615$) to assess statistical differences among different projection target regions. The brainstem, PONS, medulla and BG regions showed significantly more iNG-ET^i projections than thalamus.

(I) Correlation matrix heatmap showing pairwise Pearson correlations between ET^d and ET^i normalized fraction occupation across all areas for projections from MOs across two mice used for LightSheet Imaging.

Abbreviations: MOs – secondary motor area; FO – first order thalamic nuclei; HO- higher order thalamic nuclei; VPM – ventral posterior medial nucleus; VPL – ventral posterior lateral nucleus; PO – posterior thalamic nucleus; GPi – globus pallidus interna; PONS – pontine nuclei; BG – basal ganglia. Subregions for each target region are listed in Table S1. Scatter points in scatter plots, violin plots and box plots represent individual subregion percent occupation (normalized or raw) values, with filled markers for ipsilateral and open markers for contralateral data. Regression lines indicate overall correlation trends. Dotted grey line indicates the line of equality. Interquartile range in box plots is 25th–75th percentiles. Statistical tests used one-sample t-test, Wilcoxon signed-rank test, Kruskal–Wallis test, Wilcoxon rank-sum test and Kolmogorov-Smirnov test (p-values: *$p < 0.05$, **$p < 0.01$, ***$p < 0.001$, ****$p < 0.0001$, n.s = not significant) Scalebars in (A-G) 1 mm; (A-B right, D-F right) 500 μm; (C right) 250 μm; (G right) 100 μm.

Figure S6. Predominant ET^i over ET^d subcortical projections from VIS, Related to Figure 4

(A) AAV injection in the VIS labeled ET^d (yellow) and ET^i (magenta).

(A1) Left, location of the injection site shown on a schematic of dorsal cortex. Right, pie chart of proportion of ET^d and ET^i neurons labelled at the injection site.

(A2) Bar plots of layer-wise counts of labelled ET^d and ET^i neurons in the injection site (n = 2 mice).

(B) PT and CT fiber bundles with ET^d and ET^i projections from VIS. Notice both ET^d and ET^i projections in CT (arrowhead) while largely ET^i in PT (arrow).

(C) Dense ET^d and ET^i projections to the thalamus, including LGd/LGv.

(D) Stronger ET^i over ET^d projections to the superior colliculus.

(E) Strong ET^i but nearly no ET^d projections to the PONS.

(B1-E1) Scatter plots with linear regression of normalized fraction occupations of VIS ET^d and ET^i projections to target regions (B1) thalamus and brainstem, (C1) first order (FO) and higher order (HO) thalamus, (D1) midbrain, (E1) PONS.

(B2-E2) Violin plots showing normalized percent occupation for VIS ET^d and ET^i projections with the star indicating the median and black circles showing individual values for subregions within target regions of (B2) thalamus and brainstem, (C2) first order (FO) and higher order (HO) thalamus, (D2) midbrain, (E2) PONS.

(B3-E3) Box plots of Z-score normalized percent occupation differences between ET^i and ET^d projections from VIS to (B3) thalamus and brainstem, (C3) first order (FO) and higher order (HO) thalamus, (D3) midbrain, (E3) PONS. p-values reflect significant within region differences.

(F) Box plots of Z-score normalized percent occupation differences between ET^i and ET^d projections from VIS for brainstem, midbrain and PONS with post-hoc comparisons to thalamus, following a multiple comparisons test ($p < 0.01$) to assess statistical differences among different projection target regions. There were no significant differences between target regions.

(G) Correlation matrix heatmap showing pairwise Pearson correlations between ET^d and ET^i normalized fraction occupation across all areas for projections from VIS across two mice used for LightSheet Imaging.

Abbreviations: VIS - visual cortex; FO – first order thalamic nuclei; HO- higher order thalamic nuclei; LGd - lateral geniculate dorsal; LGv – lateral geniculate ventral; PONS – pontine nuclei. Subregions for each target region are listed in Table S1. Scatter points in scatter plots, violin plots and box plots represent individual subregion percent occupation (normalized or raw) values, with filled markers for ipsilateral and open markers for contralateral data. Regression lines indicate overall correlation trends. Dotted grey line indicates the line of equality. Interquartile range in box plots is 25th–75th percentiles. Statistical tests used one-sample t-test, Wilcoxon signed-rank test, Kruskal–Wallis test, Wilcoxon rank-sum test and Kolmogorov-Smirnov test (p-values: *$p < 0.05$, **$p < 0.01$, ***$p < 0.001$, ****$p < 0.0001$, n.s = not significant) Scalebars in (A-E) 1 mm; (A-B right, D right) 500 μm; (C right) 250 μm; (E right) 200 μm.

Figure S7. Predominant ET^i over ET^d subcortical projections from AUD, Related to Figure 4

(A) AAV injection in the AUD labeled ET^d (yellow) and ET^i (magenta).

(A1) (left) Location of the injection site shown on a schematic of dorsal cortex. (right) Pie chart of proportion of ET^d and ET^i neurons labelled at the injection site.

(A2) Bar plots of layer-wise counts of labelled ET^d and ET^i neurons in the injection site (n = 2 mice).

(B) PT and CT fiber bundles with ET^d and ET^i projections from AUD. Notice both ET^d and ET^i projections in CT (arrowhead) while largely ET^i in PT (arrow).

(C) Dense ET^d and ET^i projections to the thalamus, including MGv.

(D) Dense ET^i but weak ET^d projections to the NLLv.

(E) Stronger ET^i over ET^d projections to the inferior colliculus.

(F) Strong ET^i but weak ET^d projections to the PONS.

(G) Sparse ET^i but nearly no ET^d projections to the CN.

(B1-G1) Scatter plots with linear regression of normalized fraction occupations of AUD ET^d and ET^i projections to target regions (B1) thalamus and brainstem, (C1) first order (FO) and higher order (HO) thalamus, (D1) lemniscal sensory areas, (E1) midbrain, (F1) PONS, (G1) medulla.

(B2-G2) Violin plots showing normalized percent occupation for AUD ET^d and ET^i projections with the Star indicating the median and black circles showing individual values for subregions within target regions of (B2) thalamus and brainstem (C2) first order (FO) and higher order (HO) thalamus (D2) lemniscal sensory areas (E2) midbrain (F2) PONS (G2) medulla.

(B3-G3) Box plots of Z-score normalized percent occupation differences between ET^i and ET^d projections from AUD to (B3) thalamus and brainstem, (C3) first order (FO) and higher order (HO) thalamus, (D3) lemniscal sensory areas (E3) midbrain, (F3) PONS, (G3) medulla. p-values reflect significant within region differences.

(H) Box plots of Z-score normalized percent occupation differences between ET^i and ET^d projections from AUD for brainstem, midbrain, PONS, medulla and lemniscal sensory areas with post-hoc comparisons to thalamus, following a multiple comparisons test ($p = 0.0022$) to assess statistical differences among different projection target regions. The PONS and lemniscal sensory areas showed significantly more iNG-ET^i projections than thalamus.

(I) Correlation matrix heatmap showing pairwise Pearson correlations between ET^d and ET^i normalized fraction occupation across all areas for projections from AUD across two mice used for LightSheet Imaging.

Abbreviations: AUD – auditory cortex; FO – first order thalamic nuclei; HO- higher order thalamic nuclei; MGv – medial geniculate ventral; NLLv - nucleus of the lateral lemniscus ventral; PONS – pontine nuclei; BG – basal ganglia. Subregions for each target region are listed in Table S1. Scatter points in scatter plots, violin plots and box plots represent individual subregion percent occupation (normalized or raw) values, with filled markers for ipsilateral and open markers for contralateral data. Regression lines indicate overall correlation trends. Dotted grey line indicates the line of equality. Interquartile range in box plots is 25th–75th percentiles. Statistical tests used one-sample t-test, Wilcoxon signed-rank test, Kruskal–Wallis test, Wilcoxon rank-sum test and Kolmogorov-Smirnov test (p-values: *$p < 0.05$, **$p < 0.01$, ***$p < 0.001$, ****$p < 0.0001$, n.s = not significant) Scalebars in (A-G) 1 mm; (A-B right) 500 µm; (C right, E-G right) 200 µm; (D right) 100 µm.

Figure S8. Predominant ET^i over ET^d subcortical projections from BAR, Related to Figure 4

(A) AAV injection in the BAR labeled ET^d (yellow) and ET^i (magenta).

(A1) (left) Location of the injection site shown on a schematic of dorsal cortex. (right) Pie chart of proportion of ET^d and ET^i neurons labelled at the injection site.

(A2) Bar plots of layer-wise counts of labelled ET^d and ET^i neurons in the injection site (n = 2 mice).

(B) PT and CT fiber bundles with ET^d and ET^i projections from BAR. Notice both ET^d and ET^i projections in CT (arrowhead) while largely ET^i in PT (arrow).

(C) Dense ET^d and ET^i projections to the thalamus, including VPL/VPM/PO.

(D) Dense ET^i but weak ET^d projections to the inferior colliculus/PSV.

(E) Stronger ET^i over ET^d projections to the superior colliculus.

(F) Strong ET^i but weak ET^d projections to the PONS.

(G) Strong ET^i but weak ET^d projections to the PARN.

(B1-G1) Scatter plots with linear regression of normalized fraction occupations of BAR ET^d and ET^i projections to target regions (B1) thalamus and brainstem, (C1) first order (FO) and higher order (HO) thalamus, (D1) lemniscal sensory areas, (E1) midbrain, (F1) PONS, (G1) medulla.

(B2-G2) Violin plots showing normalized percent occupation for BAR ET^d and ET^i projections with the Star indicating the median and black circles showing individual values for subregions within target regions of (B2) thalamus and brainstem (C2) first order (FO) and higher order (HO) thalamus (D2) lemniscal sensory areas (E2) midbrain (F2) PONS (G2) medulla.

(B3-G3) Box plots of Z-score normalized percent occupation differences between ET^i and ET^d projections from BAR to (B3) thalamus and brainstem, (C3) first order (FO) and higher order (HO) thalamus, (D3) lemniscal sensory areas (E3) midbrain, (F3) PONS, (G3) medulla. p-values reflect significant within region differences.

(H) Box plots of Z-score normalized percent occupation differences between ET^i and ET^d projections from BAR for brainstem, midbrain, PONS, medulla and lemniscal sensory areas with post-hoc comparisons to thalamus, following a multiple comparisons test ($p = 0.000000000015$) to assess statistical differences among different projection target regions. The brainstem, midbrain, PONS, medulla and lemniscal sensory areas showed significantly more iNG-ET^i projections than thalamus.

(I) Correlation matrix heatmap showing pairwise Pearson correlations between ET^d and ET^i normalized fraction occupation across all areas for projections from BAR across two mice used for LightSheet Imaging.

Abbreviations: BAR – barrel cortex; FO – first order thalamic nuclei; HO- higher order thalamic nuclei; VPM – ventral posterior medial nucleus; VPL – ventral posterior lateral nucleus; PO – posterior thalamic nucleus; PONS – pontine nuclei; PSV – principal sensory nucleus of the trigeminal. Subregions for each target region are listed in Table S1. Scatter points in scatter plots, violin plots and box plots represent individual subregion percent occupation (normalized or raw) values, with filled markers for ipsilateral and open markers for contralateral data. Regression lines indicate overall correlation trends. Dotted grey line indicates the line of equality. Interquartile range in box plots is 25th–75th percentiles. Statistical tests used one-sample t-test, Wilcoxon signed-rank test, Kruskal–Wallis test, Wilcoxon rank-sum test and Kolmogorov-Smirnov test (p-values: $*p < 0.05$, $**p < 0.01$, $***p < 0.001$, $****p < 0.0001$, n.s = not significant) Scalebars in (A-G) 1 mm; (B right) 500 μm; (A right, C-F right) 200 μm; (G right) 100 μm.

Figure S9. Predominant ET^i over ET^d subcortical projections from PFC, Related to Figure 5

(A) AAV injection in the PFC labeled ET^d (yellow) and ET^i (magenta).

(A1) (left) Location of the injection site shown on a schematic of dorsal cortex. (right) Pie chart of proportion of ET^d and ET^i neurons labelled at the injection site.

(A2) Bar plots of layer-wise counts of labelled ET^d and ET^i neurons in the injection site (n = 2 mice).

(B) PT and CT fiber bundles with ET^d and ET^i projections from PFC. Notice both ET^d and ET^i projections in CT (arrowhead) while largely ET^i in PT (arrow).

(C) Dense ET^d and ET^i projections to the thalamus, including AV/AL/MD.

(D) Dense ET^i but weak ET^d projections to the olfactory tubercle.

(E) Similar ET^i and ET^d projections to the epithalamus.

(F) Strong ET^i but weak ET^d projections to the hypothalamus.

(G) Strong ET^i but weak ET^d projections to the NDB.

(H) Strong ET^i but weak ET^d projections to the superior colliculus.

(I) Strong ET^i but weak ET^d projections to the PONS.

(J) Strong ET^i but nearly no ET^d projections to the LDTN.

(B1-J1) Scatter plots with linear regression of normalized fraction occupations of PFC ET^d and ET^i projections to target regions (B1) thalamus and brainstem, (C1) first order (FO) and higher order (HO) thalamus, (D1) pallial areas, (E1) epithalamus, (F1) hypothalamus, (G1) neuromodulatory structures, (H1) midbrain, (I1) PONS, (J1) medulla.

(B2-J2) Violin plots showing normalized percent occupation for PFC ET^d and ET^i projections with the Star indicating the median and black circles showing individual values for subregions within target regions of (B2) thalamus and brainstem, (C2) first order (FO) and higher order (HO) thalamus, (D2) pallial areas, (E2) epithalamus, (F2) hypothalamus, (G2) neuromodulatory structures, (H2) midbrain, (I2) PONS, (J2) medulla.

(B3-J3) Box plots of Z-score normalized percent occupation differences between ET^i and ET^d projections from PFC to (B3) thalamus and brainstem, (C3) first order (FO) and higher order (HO) thalamus, (D3) pallial areas, (E3) epithalamus, (F3) hypothalamus, (G3) neuromodulatory structures, (H3) midbrain, (I2) PONS, (J3) medulla. p-values reflect significant within region differences.

(K) Box plots of Z-score normalized percent occupation differences between ET^i and ET^d projections from PFC for brainstem, pallium, epithalamus, hypothalamus, neuromodulatory structures, midbrain, PONS and medulla with post-hoc comparisons to thalamus, following a multiple comparisons test ($p = 0.000000135$) to assess statistical differences among different projection target regions. The brainstem, pallium, hypothalamus, neuromodulatory structures, midbrain, PONS and medulla areas showed significantly more iNG-ET^i projections than thalamus.

(L) Correlation matrix heatmap showing pairwise Pearson correlations between ET^d and ET^i normalized fraction occupation across all areas for projections from PFC across two mice used for LightSheet Imaging.

Abbreviations: PFC – prefrontal cortex; FO – first order thalamic nuclei; HO- higher order thalamic nuclei; VPM – ventral posterior medial nucleus; AV – anteroventral nucleus; AM – anteromedial nucleus; MD – mediodorsal nucleus of thalamus; NDB – nucleus of the diagonal band; LDTN – lateral dorsal tegmental nucleus; PONS – pontine nuclei. Subregions for each target region are listed in Table S1. Scatter points in scatter plots, violin plots and box plots represent individual subregion percent occupation (normalized or raw) values, with filled markers for ipsilateral and open markers for contralateral data. Regression lines indicate overall correlation trends. Dotted grey line indicates the line of equality. Interquartile range in box plots is 25th–75th percentiles. Statistical tests used one-sample t-test, Wilcoxon signed-rank test, Kruskal–Wallis test, Wilcoxon rank-sum test and Kolmogorov-Smirnov test (p-values: *$p < 0.05$, **$p < 0.01$, ***$p < 0.001$, ****$p < 0.0001$, n.s = not significant) Scalebars in (A-J) 1 mm; (B right) 500 µm; (A right, C-D right, F-J right) 200 µm; (E right) 100 µm.

Figure S10. Predominant ET^i over ET^d subcortical projections from PAR, Related to Figure 5

(A) AAV injection in the PAR labeled ET^d (yellow) and ET^i (magenta).

(A1) (left) Location of the injection site shown on a schematic of dorsal cortex. (right) Pie chart of proportion of ET^d and ET^i neurons labelled at the injection site.

(A2) Bar plots of layer-wise counts of labelled ET^d and ET^i neurons in the injection site (n = 2 mice).

(B) PT and CT fiber bundles with ET^d and ET^i projections from PAR. Notice both ET^d and ET^i projections in CT (arrowhead) while largely ET^i in PT (arrow).

(C) Dense ET^d and ET^i projections to the thalamus, including VPL/VPM/VA.

(D) Dense ET^i but weak ET^d projections to the GPe.

(E) Stronger ET^i over ET^d projections to the superior colliculus.

(F) Strong ET^i but weak ET^d projections to the PONS.

(G) Strong ET^i but nearly no ET^d projections to the spinal cord.

(B1-G1) Scatter plots with linear regression of normalized fraction occupations of PAR ET^d and ET^i projections to target regions (B1) thalamus and brainstem, (C1) first order (FO) and higher order (HO) thalamus, (D1) basal ganglia, (E1) midbrain, (F1) PONS, (G1) medulla.

(B2-G2) Violin plots showing normalized percent occupation for PAR ET^d and ET^i projections with the Star indicating the median and black circles showing individual values for subregions within target regions of (B2) thalamus and brainstem (C2) first order (FO) and higher order (HO) thalamus (D2) basal ganglia (E2) midbrain (F2) PONS (G2) medulla.

(B3-G3) Box plots of Z-score normalized percent occupation differences between ET^i and ET^d projections from PAR to (B3) thalamus and brainstem, (C3) first order (FO) and higher order (HO) thalamus, (D3) basal ganglia, (E3) midbrain, (F3) PONS, (G3) medulla. p-values reflect significant within region differences.

(H) Box plots of Z-score normalized percent occupation differences between ET^i and ET^d projections from PAR for brainstem, midbrain, PONS, medulla and BG with post-hoc comparisons to thalamus, following a multiple comparisons test ($p = 0.0001$) to assess statistical differences among different projection target regions. The brainstem, PONS and medulla regions showed significantly more iNG-ET^i projections than thalamus.

(I) Correlation matrix heatmap showing pairwise Pearson correlations between ET^d and ET^i normalized fraction occupation across all areas for projections from PAR across two mice used for LightSheet Imaging.

Abbreviations: PAR – parietal cortex; FO – first order thalamic nuclei; HO- higher order thalamic nuclei; VPM – ventral posterior medial nucleus; VPL – ventral posterior lateral nucleus; VAL – ventral anterio-lateral complex of thalamus; GPe – globus pallidus externa; PONS – pontine nuclei; BG – basal ganglia. Subregions for each target region are listed in Table S1. Scatter points in scatter plots, violin plots and box plots represent individual subregion percent occupation (normalized or raw) values, with filled markers for ipsilateral and open markers for contralateral data. Regression lines indicate overall correlation trends. Dotted grey line indicates the line of equality. Interquartile range in box plots is 25th–75th percentiles. Statistical tests used one-sample t-test, Wilcoxon signed-rank test, Kruskal–Wallis test, Wilcoxon rank-sum test and Kolmogorov-Smirnov test (p-values: *$p < 0.05$, **$p < 0.01$, ***$p < 0.001$, ****$p < 0.0001$, n.s = not significant) Scalebars in (A-G) 1 mm; (B right) 500 µm; (G right) 400 µm; (A right,C-F right) 200 µm.

Figure S11. Developing ET^i neurons across cerebral cortical structures initially all project axons to the spinal cord. Related to Figure 6

(A-C) Spinal-projecting neurons retrogradely labelled from injections to cSpC of P4 mice and harvested at P40 (P4-P40) in (A) piriform cortex (B) BLA (C) Hippocampus – CA1 & subiculum. Note almost all of the labelled nuclei are ET^i.

(D) Correlation matrix heatmap showing pairwise Pearson correlations between ET^d and ET^i nuclei retrogradely labelled from cSpC in P4-P40 mice, across different non-isocortical pallial areas from two mice used for LightSheet Imaging.

(E) Bar plots of retrogradely labelled spinal-projecting ET^d (yellow) and ET^i (magenta) nuclei numbers across different non-isocortical pallial areas labelled from injections into cSpC in P4-P40 mice. Zoomed in sections (dotted black box) of the bar plots showing small to zero number of ET^d with the longer bar of ET^i which exceeds the zoomed scale truncated.

(F) Proportions of spinal-projecting ET^d (yellow) and ET^i (magenta) nuclei across different non-isocortical pallial areas in P4-P40 mice.

(G) Number of retrogradely labelled corticospinal ET^i are significantly more than ET^d across different non-isocortical pallial areas in P4-P40 mice.

(H) Sparse labelling of retrogradely labelled spinal-projecting ET^d and ET^i neurons in the isocortex from injections into cSpC in P1-P40 mice.

(I) Retrogradely labelled spinal-projecting ET^d and ET^i neurons in the isocortex and BLA from injections of generic retro-AAV into cSpC of P6 wildtype mice and harvested at P40 (P6-P40).

Abbreviations: BLA – basolateral amygdala; CA1 – Cornu Ammonis area 1; cSpC – cervical spinal cord. P1-P40 – injected in P1 and harvested at P40; P4-P40 – injected in P4 and harvested at P40; P28-P40 – injected in P28 and harvested at P40 Subregions in (E) are listed in Table S1. Statistical tests used: two-sample t-test, (p-values: ****$p < 0.0001$) Scalebars in (A-C, H-I) 1 mm; (C middle, H right) 500 µm; (B right, C right, I right) 200 µm..

Supplementary Videos

Supplementary Video 1. Whole-brain Lightsheet image stack of retrogradely labelled ET^d (yellow) and ET^i (magenta) neurons across the isocortex from injections into the superior colliculus(SC) in a FezF2TC;Tbr2Flp mouse.

Supplementary Video 2. Whole-brain Lightsheet image stack of retrogradely labelled ET^d (yellow) and ET^i (magenta) neurons across the isocortex from injections into the pontine nuclei (PONS) in a FezF2TC;Tbr2Flp mouse.

Supplementary Video 3. Whole-brain Lightsheet image stack of retrogradely labelled ET^d (yellow) and ET^i (magenta) neurons across the isocortex from injections into the medulla (MED) in a FezF2TC;Tbr2Flp.

Supplementary Video 4. Whole-brain Lightsheet image stack of retrogradely labelled ET^d (yellow) and ET^i (magenta) neurons across the isocortex from injections into the cervical spinal cord (cSpC) in a FezF2TC;Tbr2Flp mouse.

Supplementary Video 5. Whole-brain Lightsheet image stack of anterograde axonal projections of ET^d (yellow) and ET^i (magenta) neurons in the rostral forelimb orofacial area (RFO) of the isocortex in a FezF2TC;Tbr2Flp mouse.

Supplementary Video 6. Whole-brain Lightsheet image stack of anterograde axonal projections of ET^d (yellow) and ET^i (magenta) neurons in the caudal forelimb area (CFA) of the isocortex in a FezF2TC;Tbr2Flp mouse.

Supplementary Video 7. Whole-brain Lightsheet image stack of anterograde axonal projections of ET^d (yellow) and ET^i (magenta) neurons in the secondary motor area (MOs) of the isocortex in a FezF2TC;Tbr2Flp mouse.

Supplementary Video 8. Whole-brain Lightsheet image stack of anterograde axonal projections of ET^d (yellow) and ET^i (magenta) neurons in the visual cortex (VIS) in a FezF2TC;Tbr2Flp mouse.

Supplementary Video 9. Whole-brain Lightsheet image stack of anterograde axonal projections of ET^d (yellow) and ET^i (magenta) neurons in the auditory cortex (AUD) in a FezF2TC;Tbr2Flp mouse.

Supplementary Video 10. Whole-brain Lightsheet image stack of anterograde axonal projections of ET^d (yellow) and ET^i (magenta) neurons in the barrel cortex (BAR) in a FezF2TC;Tbr2Flp mouse.

Supplementary Video 11. Whole-brain Lightsheet image stack of anterograde axonal projections of ET^d (yellow) and ET^i (magenta) neurons in the prefrontal cortex (PFC) in a FezF2TC;Tbr2Flp mouse.

Supplementary Video 12. Whole-brain Lightsheet image stack of anterograde axonal projections of ET^d (yellow) and ET^i (magenta) neurons in the parietal cortex (PAR) in a FezF2TC;Tbr2Flp mouse.

Supplementary Video 13. Whole-brain Lightsheet image stack of retrogradely labelled ET^d (yellow) and ET^i (magenta) nuclei across different cortical/pallial areas from injections into the cervical spinal cord (cSpC) of a P4 FezF2TC;Tbr2Flp mouse and harvested at P40 (P4-P40).